Journal of Sound and Vibration 627 (2026) 119657

Contents lists available at ScienceDirect

Journal of Sound and Vibration

journal homepage: www.elsevier.com/locate/jsvi

Vibration-weighted maximum correlated kurtosis deconvolution and latent cyclic pattern discovery for fault diagnosis of high-speed rail bogies

Peng Chen [a,b], Yuhao Wu [a], Junxiao Ma [a], Ruijin Zhang [a], Ge Xin [c], Changbo He [d,*]

[a] College of Engineering, Shantou University, Shantou, 515063, Guangdong, PR China
[b] Key Laboratory of Intelligent Manufacturing Technology, Ministry of Education, Shantou, 515063, Guangdong, PR China
[c] School of Traffic and Transportation, Beijing Jiaotong University, Beijing, 100044, PR China
[d] College of Electrical Engineering and Automation, Anhui University, Hefei, 230601, PR China

ARTICLE INFO

Keywords:
High-speed rail bogie
Multi-source
Compound fault diagnosis
Multi-source vibration demodulation
Condition monitoring
Prognostics and health management

ABSTRACT

Real-world high-speed rail bogie vibration signals combine mechanical oscillations, deterministic periodic components (e.g., gear-mesh harmonics and wheel-rail interactions), environmental noise, and transients, making fault features hard to isolate. Diagnosis is further hindered by manual hyperparameter tuning, weak impulsive signatures at low Signal-to-Noise Ratio (SNR), overlapping spectral-temporal content with mode mixing, and high computational cost on long multichannel records. We propose a multi-source vibration demodulation framework–an optimized Maximum Correlated Kurtosis Deconvolution (MCKD) with vibration-weighted grading distribution and Latent Cyclic Pattern Discovery (LCPD). The method couples spectral-negentropy-driven adaptivity for Minimum Entropy Deconvolution (MED)/MCKD filter length and regularization with wavelet-packet multiscale decomposition guided by correlation-kurtosis band selection, and periodic dynamic windows with a Vibration Amplitude-based Grading and Weighting Distribution (VAGWD), enabling adaptive deconvolution, enhanced weak-impulse extraction, and cycle-synchronous separation and quantification without empirical tuning. The LCPD module exploits envelope-cepstral cues, squared-envelope autocorrelation, and cyclic spectral coherence to recover hidden or time-warped periodicities under compound-fault conditions. Experiments on bogie datasets show higher diagnostic accuracy, greater noise robustness, and improved computational efficiency than MED, Multipoint Optimal Minimum Entropy Deconvolution Adjusted (MOMEDA), and baseline MCKD, enabling reliable and efficient compound-fault diagnosis in high-speed rail bogies.

1. Introduction

The high-speed rail system exemplifies an exceptionally sophisticated and intricately coupled mechanical network, wherein the bogie system functions as an indispensable component of railway rolling stock [1–4]. This critical subsystem assumes a fundamental role in maintaining both operational safety and reliability throughout the railway infrastructure. Within this complex framework, bogie

* Corresponding author.
E-mail addresses: pengchen@alu.uestc.edu.cn, dr.pengchen@foxmail.com (P. Chen), changbh@ahu.edu.cn (C. He).

https://doi.org/10.1016/j.jsv.2026.119657
Received 19 August 2025; Received in revised form 22 December 2025; Accepted 8 January 2026
Available online 11 January 2026

axle bearings and gears are continuously subjected to substantial mechanical loads and diverse environmental stressors during sustained high-velocity operations. Furthermore, due to the inherent complexity of the structural design and the challenging operational conditions, compound faults frequently manifest within bogie systems, demonstrating a cascading effect whereby bearing deterioration can precipitate gear failures, and localized gear damage can progressively lead to comprehensive mechanical breakdown. The concurrent detection of multiple faults within bogie system components holds paramount significance, as it enables both the precise identification of fault origins and the strategic scheduling of maintenance interventions. Moreover, considering that malfunctions in bogie axle bearings and gears potentially culminate in catastrophic consequences for railway operations and passenger safety, the implementation of robust fault monitoring protocols and predictive maintenance frameworks becomes imperative. Through the systematic integration of these proactive measures, railway operators can effectively preserve operational integrity while substantially minimizing safety risks.

In high-speed rail system and industrial applications, practitioners frequently encounter substantial challenges in the detection and precise diagnosis of compound faults, particularly due to the sophisticated and intricate interactions between multiple fault characteristics emanating from diverse vibration sources, which are invariably obscured by omnipresent background noise in mechanical systems [5–9]. A quintessential example of this complexity manifests in bearing-gear fault scenarios, where the characteristic frequency signatures of bearing defects exhibit a tendency to coincide with or closely approximate the higher-order harmonics of gear fault frequencies, thereby creating a formidable barrier to the direct discrimination and isolation of these distinct fault patterns. Moreover, the inherent diagnostic complexity is further exacerbated by the fact that bearing fault signatures are frequently overwhelmed by the substantially more energetic vibrations generated during gear mesh interactions, thus presenting an additional layer of challenge in achieving reliable fault identification. In light of these multifaceted challenges, the scientific community has responded with the development and implementation of sophisticated diagnostic methodologies, encompassing advanced signal processing techniques such as Blind Deconvolution (BD) [10–13], Wavelet Transform (WT) analysis [14–16], and Sparse Representation (SR) [17,18], all of which have been specifically engineered and refined to facilitate the extraction and precise identification of fault characteristics, even in the presence of confounding noise and overlapping signal patterns that typify real-world mechanical systems.

In the evolutionary landscape of mechanical fault diagnosis, deconvolution methods have emerged as powerful tools for fault impact signal recovery through iterative filter optimization aimed at achieving optimal output signal evaluation indices [19,20]. This methodological progression began with Wiggins' groundbreaking introduction of the Minimum Entropy Deconvolution (MED) [21] method, which established fundamental principles for blind source separation and was subsequently adapted by Sawalhi et al. [22] for bearing fault diagnosis with notable success. However, the conventional MED method's reliance on kurtosis index as an objective function revealed limitations when applied to vibration signals characterized by random impacts. In response to these constraints, McDonald et al. [23] advanced the field by introducing the concept of Correlated Kurtosis (CK) and developing the Maximum Correlation Kurtosis Deconvolution (MCKD) method, which effectively addressed the MED's susceptibility to random impact noise through innovative periodic filter design and optimization techniques. Despite these advancements, the MCKD method's effectiveness remained somewhat limited by its dependence on experiential parameter selection, highlighting the need for adaptive parameter determination approaches. As such, McDonald et al. significantly advanced the field of mechanical fault diagnosis by introducing the innovative concept of multiple D norm and developing the Multipoint optimal Minimum Entropy Deconvolution Adjusted (MOMEDA) [24] method. This approach excels at detecting periodic fault impact signals, yet its efficacy is notably compromised under conditions of intense background noise, which severely hampers diagnostic accuracy. To address the challenge of identifying weak fault features amidst such noise, Buzzoni and Antoni [25] proposed an alternative technique grounded in maximum second-order Cyclostationary Blind Deconvolution (CYCBD), which demonstrates a robust capacity to isolate the impact components of weak faults from measured signals. Unlike traditional deconvolution strategies, where methods like MED are limited to recovering only a single dominant pulse and MCKD can extract merely a restricted number of pulses, CYCBD effectively captures continuous periodic pulses, thereby offering a substantial improvement. Furthermore, when compared to MOMEDA, CYCBD not only extracts these periodic pulses but also amplifies them, achieving superior noise suppression. Nevertheless, the effectiveness of CYCBD is heavily contingent upon the precise calibration of cycle frequency, a parameter that remains critical to its performance. Although recent research has increasingly relied on metaheuristic optimization algorithms to fine-tune CYCBD parameters, the associated computational inefficiency poses a significant barrier, particularly in meeting the stringent demands of high-speed train condition monitoring where rapid processing is essential.

Furthermore, the signal processing methodologies for fault detection and diagnosis have witnessed significant advancements beyond the traditional SK method and deconvolution techniques, particularly in the domain of decomposition-based approaches. These methods systematically segregate various signal components into distinct modes using predefined criteria, with notable examples including Empirical Mode Decomposition (EMD) [26] and its subsequent derivatives [27,28], as well as Variational Mode Decomposition (VMD) [29] and its advanced iterations [30,31]. Such decomposition techniques have emerged as particularly promising solutions for extracting early fault features in scenarios characterized by multi-component modulation and complex interference patterns, thereby addressing challenges that conventional methods struggle to resolve. Nevertheless, these optimization-driven approaches are not without their inherent limitations; most notably, they frequently encounter computational bottlenecks due to their intensive processing requirements and demonstrate a pronounced susceptibility to becoming trapped in local extrema, which can significantly compromise their effectiveness in real-world applications where computational efficiency and reliable global optimization are paramount considerations.

Despite significant advances in vibration analysis methodologies for fault diagnosis and detection in high-speed rail system, particularly in bogie system, several fundamental challenges persist and warrant comprehensive investigation.

1. Conventional deconvolution methods and decomposition pipelines are heavily dependent on manually tuned hyper-parameters (e.g. filter length, regularization, and band selection). This lack of adaptability leads to suboptimal performance when encountering complex, multi-source vibration responses from bogie systems operating under compound fault conditions.
2. Methods such as MOMEDA and classical MED often exhibit limited sensitivity to weak impulsive signatures at low signal-to-noise ratios, especially when impulses are masked by energetic deterministic components (e.g., gear-mesh harmonics, wheel-rail periodicities), thereby increasing the risk of missed detections and misclassification.
3. Existing approaches struggle to disentangle coexisting fault signatures with overlapping spectral-temporal support, and decomposition-based techniques are prone to mode mixing and leakage, incurring substantial computational overhead for long-duration, multi-channel recordings and thereby constraining real-time applicability.

To address these gaps, we propose a multi-source vibration demodulation framework–an optimized MCKD with vibration-weighted grading distribution and latent cyclic pattern discovery. It leverages spectral negentropy to adaptively set filter lengths and regularization (eliminating manual tuning), couples wavelet-packet multiscale decomposition with correlation kurtosis to enhance weak-impulse extraction under strong noise, and employs periodic dynamic windows with vibration-weighted grading to separate and quantify overlapping fault features, while Latent Cyclic Pattern Discovery (LCPD) recovers hidden or time-warped periodicities under compound fault scenarios collectively enabling reliable and efficient compound-fault diagnosis in bogie systems.

1. The framework integrates spectral negentropy to adaptively determine MED/MCKD filter lengths and regularization strength, thereby eliminating reliance on empirical settings, aligning the filter support with periodicities specific to vibration sources, and enhancing robustness across heterogeneous fault mechanisms in bogie systems.
2. By combining wavelet-packet multiscale decomposition with correlation-kurtosis-guided band selection, the method strengthens the extraction of weak periodic impulses, markedly improving anti-noise performance under strong background interference and mitigating the impact of nonstationary operational conditions.
3. The introduction of periodic dynamic windows together with Vibration Amplitude-based Grading and Weighting Distribution (VAGWD) enables cycle-synchronous separation and quantitative attribution of overlapping fault features, thereby improving the reliability and interpretability of compound fault diagnosis.

This research paper is organized to provide a coherent and detailed exploration of its robust methodology and key findings, ensuring that readers can navigate the complex subject matter with clarity. At the outset, Section 2 offers an in-depth analysis of the underlying theoretical framework, placing particular emphasis on Minimum Entropy Deconvolution (MED) as a critical foundation, thereby equipping readers with the essential conceptual tools to appreciate the innovative advancements that follow. Building upon this, Section 3 introduces the key methodological contribution of the study–an advanced iteration of the Maximum Correlated Kurtosis Deconvolution (MCKD) framework–which integrates cutting-edge features such as vibration weighted grading distribution and latent cyclic pattern discovery, thus marking a notable leap forward in the precision and reliability of fault detection and signal processing within railway bogie system diagnostics. Moreover, the practical implications and robustness of this proposed methodology are rigorously evaluated in Section 4, which includes a comprehensive comparative analysis supported by two distinct empirical case studies elaborated in Sections 4.3 and 4.2, thereby affirming the framework's real-world utility and effectiveness. Finally, the paper concludes in Section 5 by synthesizing the definitive outcomes of the research while also delineating potential avenues for future inquiry, offering a balanced and forward-looking perspective on both the immediate impacts and the broader possibilities for development within this specialized domain of study.

2. Related theory

The MED [21] technique, initially developed for seismic signal processing and subsequently adapted for mechanical fault diagnosis, represents an advanced signal processing technique engineered to enhance the periodic impulsive component of a signal through the design of an optimal Finite Impulse Response (FIR) filter. The algorithm accomplishes this enhancement indirectly by maximizing the kurtosis of the output signal, whereby a higher kurtosis inherently indicates the prevalence of more extreme values or impulsive components in the signal, thus facilitating the detection of mechanical failures.

In the field of mechanical systems analysis, when examining a time-domain vibration signal $\mathbf{x}$, it can be decomposed into four fundamental constituents: the fault-induced impulse component $\mathbf{u}$, the harmonic component $\mathbf{d}$, the stochastic white noise component $\mathbf{n}_w$, and the transient non-Gaussian noise component $\mathbf{n}_t$. Consequently, the measured vibration signal $\mathbf{x}$ can be mathematically expressed as:

$$\mathbf{x} = \mathbf{h}_w * \mathbf{u} + \mathbf{h}_d * \mathbf{d} + \mathbf{h}_{n_w} * \mathbf{n}_w + \mathbf{h}_{n_t} * \mathbf{n}_t \tag{1}$$

In this mathematical framework, referring to Eq. (1), the constituent components are defined as follows: The mathbftor $\mathbf{x} = [x_1, x_2, \dots, x_N]^T$ represents the measured vibration signal, which encompasses the entirety of the system's mechanical response and serves as the primary input for analysis. The fault-induced impulse sequence $\mathbf{u} = [u_1, u_2, \dots, u_N]^T$ manifests as a series of sparse and periodic pulses, which are characteristic signatures of mechanical defects or anomalies within the system. These impulses are particuluarly significant as they often provide crucial diagnostic information about the system's condition. The harmonic component $\mathbf{d} = [d_1, d_2, \dots, d_N]^T$ emerges from the rotational elements within the mechanical system. This component can be mathematically decomposed into a superposition of multiple sinusoidal waves, each corresponding to specific mechanical frequencies inherent to the system's operation. The noise component $\mathbf{n_w} = [n_{w1}, n_{w2}, \dots, n_{wN}]^T$ represents the unavoidable presence of zero-mean Gaussian white

noise, characterized by its uniform power spectral density across all frequencies. This type of noise is inherent in all measurement systems and must be carefully considered in the analysis. The transient non-Gaussian noise component $\mathbf{n}_t = [n_{t1}, n_{t2}, \ldots, n_{tN}]^T$ accounts for irregular disturbances stemming from external interference or environmental factors. This component is distinguished by its high kurtosis value and its non-stationary nature, making it particularly challenging to filter out. The system's dynamic response characteristics are captured through the transmission path effects $\mathbf{h}_u$, $\mathbf{h}_d$, $\mathbf{h}_{n_w}$, and $\mathbf{h}_{n_t}$, which correspond to the fault, harmonic, white noise, and transient non-Gaussian noise components respectively. These effects are modeled as finite impulse response (FIR) filters, with the operator $*$ denoting the convolution operation between the respective signals and their transmission paths.

Given this comprehensive signal composition, the primary objective of Minimum Entropy Deconvolution (MED) is to effectively isolate and extract the original impulse sequence $\mathbf{u}$ from the composite input signal $\mathbf{x}$. This extraction process must simultaneously suppress the influences of harmonic components, white noise, and transient non-Gaussian noise to achieve optimal signal separation.

The implementation of MED relies on an iterative optimization process to determine the final filter $\mathbf{f}$. During each iteration, the current filter estimate $\mathbf{f}^{(k)}$ is convolved with the input signal $\mathbf{x}$ to generate an intermediate output signal $\mathbf{y}^{(k)}$.

$$\mathbf{y}^{(k)} = \sum_{l=1}^{L} f_l^{(k)} x_{n+l-1} \tag{2}$$

where k represents the number of iteration, L is the length of the filter, $n = 1, 2, \ldots, N - L + 1$.

Subsequently, the statistical properties of the output signal $\mathbf{y}^{(k)}$ are computed through the following relationship:

$$S_i^{(k)} = \sum_{n=1}^{N-L+1} \left(y_n^{(k)}\right)^i \tag{3}$$

To achieve the iterative update of the filter, it is essential to first construct the embedding matrix $\mathbf{X}_m$ of the input signal $\mathbf{x}$. T his matrix acts as the core computational carrier for mapping the one-dimensional vibration signal into a high-dimensional space, providing the basis for subsequent filter-signal convolution and statistic integration. Specifically, $\mathbf{X}_m$ has dimensions $(N - L + 1) \times L$ (where N is the length of the input signal $\mathbf{x}$, and L is the length of the FIR filter), and each row corresponds to a delayed version of the signal to fully preserve the temporal correlation of the vibration signal. Its specific structure is defined as:

$$\mathbf{X}_m = \begin{bmatrix} x_1 & x_2 & \cdots & x_L \\ x_2 & x_3 & \cdots & x_{L+1} \\ \vdots & \vdots & \ddots & \vdots \\ x_{N-L+1} & x_{N-L+2} & \cdots & x_N \end{bmatrix} \tag{4}$$

With the computed statistics $S_i^{(k)}$ and the pre-constructed embedding matrix $\mathbf{X}_m$, the filter $\mathbf{f}^{(k+1)}$ can be iteratively updated to optimize its impulse extraction performance. The update formula is given by:

$$\mathbf{f}^{(k+1)} = \frac{S_2^{(k)}}{S_4^{(k)}} \left(\mathbf{X}_m^{\mathrm{T}} \mathbf{X}_m\right)^{-1} \mathbf{X}_m^{\mathrm{T}} (\mathbf{y}^{(k)})^3 \tag{5}$$

Through successive iterations, the filter $\mathbf{f}$ converges asymptotically toward an optimal solution that maximizes the kurtosis of the output signal $\mathbf{y}$. The final optimized filter $\mathbf{f}$ can be mathematically expressed in its complete form as:

$$\mathbf{f} = \left(\mathbf{X}_m^{\mathrm{T}} \mathbf{X}_m\right)^{-1} \mathbf{X}_m^{\mathrm{T}} \cdot \frac{\mathbf{y}^3}{\|\mathbf{y}^2\|_2^2} \tag{6}$$

3. An optimized maximum correlated Kurtosis deconvolution (MCKD) framework with vibration weighted grading distribution and latent cyclic pattern discovery

In the domain of signal processing methodologies, while the MED [21] technique has shown promise in enhancing and extracting periodic vibration components from signals, a critical examination of its inherent constraints reveals several noteworthy limitations. Of particular significance is the method's performance in complex scenarios involving multiple vibration sources, wherein its effectiveness becomes heavily dependent on precise parameter configurations, thus demanding rigorous analytical calibration. Furthermore, the susceptibility of MED to interference from multi-source noise emerges as a substantial impediment, especially when analyzing compound fault signals within sophisticated mechanical systems. To overcome these challenges, this research proposes a MCKD framework that synthesizes an enhanced minimum negative entropy deconvolution approach with innovative methodological components, specifically incorporating vibration-weighted hierarchical distributions and latent cyclic pattern discovery mechanisms. Through the integration of these analytical techniques, our framework facilitates the precise identification and isolation of signals emanating from diverse fault sources within complex compound signals. Consequently, this refined methodology not only augments fault detection precision but also substantially enhances the framework's robustness and adaptability in challenging signal environments. The architectural composition of this novel framework, encompassing its interconnected analytical elements and their sequential implementation protocol, is illustrated in Fig. 1.

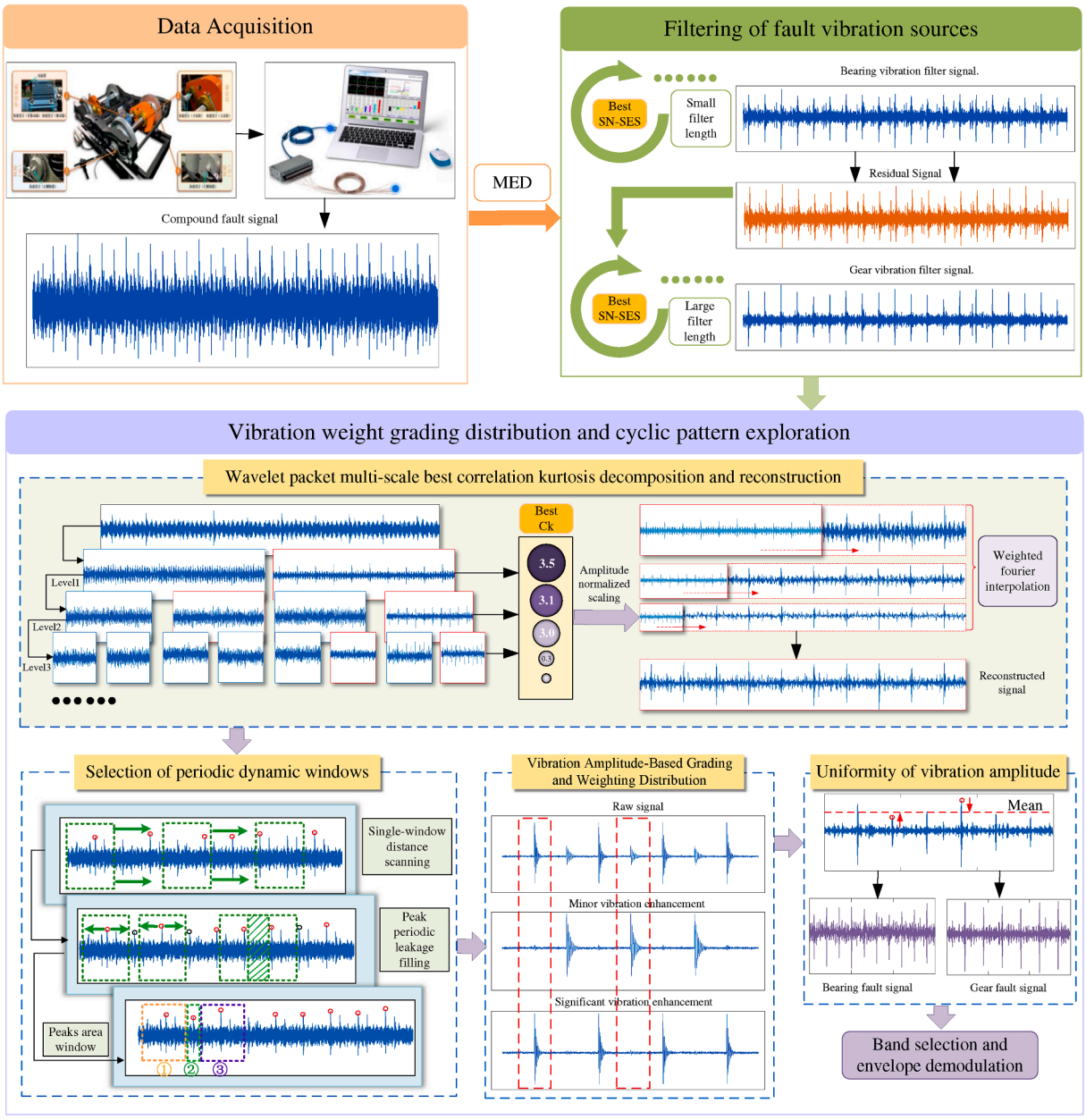

Fig. 1. The diagram of proposed method for vibration weighted grading distribution and latent cyclic pattern discovery.

3.1. Adaptive adjustment of MED filter length for vibration source optimization

3.1.1. Quantifying uncertainty in frequency bands: Spectral negentropy

Spectral negentropy is a critical parameter employed to measure the degree of uncertainty or irregularity in a signal within a specific frequency band. It is particularly relevant for the analysis of non-stationary signals characterized by periodic impulses. The presence of impulsive components within vibration signals can be interpreted as deviations from the system's equilibrium state, which are observable as localized energy fluctuations in the time domain. These fluctuations lead to a reduction in the Spectral Negentropy of the Squared Envelope (SN-SE). Conversely, if the energy fluctuations exhibit periodic properties, as reflected in the envelope spectrum, this indicates localized energy variations in the frequency domain, resulting in a prominent peak at a specific frequency. This phenomenon leads to an increase in the Spectral Negentropy of the Squared Envelope Spectrum (SN-SES), indicating such periodic fluctuations. The mathematical formulation for the spectral negentropy measures SN-SE and SN-SES can be expressed as:

$$\Delta I_\epsilon = -H_\epsilon(f,\Delta f) = \langle \frac{\varepsilon_x(n,f,\Delta f)^2}{\langle \varepsilon_x(n,f,\Delta f)^2\rangle} \ln\left[\frac{\varepsilon_x(n,f,\Delta f)^2}{\langle \varepsilon_x(n,f,\Delta f)^2\rangle}\right]\rangle \tag{7}$$

$$\Delta I_E = -H_E(f,\Delta f) = \langle \frac{E_x(a,f,\Delta f)^2}{\langle E_x(a,f,\Delta f)^2\rangle} \ln\left[\frac{E_x(a,f,\Delta f)^2}{\langle E_x(a,f,\Delta f)^2\rangle}\right]\rangle \tag{8}$$

where $\langle\cdot\rangle$ denotes the average operator, n represents discrete time points, and f represents frequency points. $\varepsilon_x(n,f,\Delta f) = |x(n,f,\Delta f)|^2$ is the square envelope of a discrete signal $x(n)(n=0,\dots,L)$ within the frequency band range of $[f-\Delta f/2, f+\Delta f/2]$. $E_x(\alpha,f,\Delta f) = \sum_{n=0}^{L-1} \epsilon_x(n,f,\Delta f)\exp^{-j2\pi an/f_s}$ is the square envelope of the discrete signal within the frequency band range of $[f-\Delta f/2, f+\Delta f/2]$. f_s is the sampling frequency.

During stable operation, the spectral negative entropy of the vibration signal maintains a consistent minimal value. However, the onset of equipment degradation or fault conditions manifests through characteristic periodic impulses in the time-domain waveform, precipitating a measurable increase in spectral negentropy values, accompanied by concurrent elevations in both ΔI_ϵ and ΔI_E measurements. While random impulses become discernible within the signal's squared envelope, their manifestation remains significantly attenuated within the squared envelope's spectral domain. This fundamental differentiation underscores the superior diagnostic capabilities of both ΔI_ϵ and ΔI_E metrics in periodic impulse detection, with ΔI_E demonstrating particularly noteworthy advantages through its inherent capacity to mitigate random impulse interference. Consequently, given this enhanced discriminatory capability, ΔI_E emerges as an exceptionally robust and reliable metric for narrowband signal feature extraction, particularly when analyzing complex scenarios characterized by compound fault conditions and elevated noise levels prevalent in industrial applications. Furthermore, the square envelope spectral value ΔI_E distinguishes itself as the optimal entropy criterion, owing to its demonstrated proficiency in minimizing random fluctuation-induced distortions, thereby substantially augmenting the overall reliability and precision of signal analysis in practical diagnostic applications.

3.1.2. Adaptive optimization of MED filter parameters through SN-SES based dual-component analysis

The detection and analysis of composite fault signals in mechanical systems, particularly those involving both gears and bearings, requires advanced signal processing techniques for accurate fault feature extraction. This research presents an innovative methodology that adaptively modifies the Minimum Entropy Deconvolution (MED) filter length using a spectral negentropy selection criterion, thereby optimizing the extraction of fault features from complex mechanical signals. In composite fault scenarios, gear assembly failures typically manifest as prominent impact amplitudes within the signal. This characteristic necessitates using an extended MED filters. Consequently, the methodology begins by defining the gear fault frequency band as a multiple of the meshing frequency, expressed as $\Delta f^{\text{gear}} = [1, n\times f_m]$, where n is set to 3 in the current implementation. The process involves iterative evaluation through a range of candidate MED filter lengths defined by $L_g = [L_{\min}^{\text{gear}} : l_{\text{step}} : L_{\max}^{\text{gear}}]$, with parameters $L_{\min}^{\text{gear}} = 20$, $L_{\max}^{\text{gear}} = 200$, and $l_{\text{step}} = 5$.

For each filter length L_g, the original vibration signal $x(t)$ undergoes MED processing to produce a screened gear signal $y_{L_g}(t)$, as represented by the Eq. (9):

$$y_{L_g}(t) = \text{MED}(x(t), L_g) \tag{9}$$

Subsequently, the SN-SES value is computed for the enhanced gear signal within the predetermined frequency band $\Delta I_{E,L_g}^{\text{gear}}$, following:

$$\Delta I_{E,L_g}^{\text{gear}} = \text{SN-SES}(y_{L_g}(t), f_s, \Delta f^{\text{gear}}) \tag{10}$$

The algorithm continuously updates the maximum SN-SES value and corresponding optimal filter length $L_{\text{best}}^{\text{gear}}$ when superior results are encountered during iteration. Upon completion of the traversal process, the system identifies the optimal filter length $L_{\text{best}}^{\text{gear}}$ and generates the corresponding enhanced gear signal $y_{\text{best}}^{\text{gear}}(t)$.

The analysis then progresses to isolating potential bearing fault characteristics by deriving a residual signal. This is accomplished by subtracting the enhanced gear signal components from the original signal, as shown in:

$$r(t) = x(t) - y_{\text{best}}^{\text{gear}}(t) \tag{11}$$

The bearing fault analysis follows an analogous methodology, albeit with modified parameters to accommodate the unique characteristics of bearing signals. Specifically, the SN-SES frequency band undergoes a systematic recalibration to $\Delta f^{\text{bearing}} = [1, n\times BPFI]$, while the MED filter implementation incorporates a more narrowly defined filter length range $L_b = [L_{\min}^{\text{bearing}} : l_{\text{step}} : L_{\max}^{\text{bearing}}]$, wherein the parameters are precisely constrained by $L_{\min}^{\text{bearing}} = 2$, $L_{\max}^{\text{bearing}} = 50$, and $l_{\text{step}} = 1$. Through a rigorous iterative optimization protocol, the methodology systematically determines the optimal SN-SES value $\Delta I_{E,L_b}^{\text{bearing}}$ and subsequently generates the enhanced bearing signal $y_{\text{best}}^{\text{bearing}}$. This sophisticated analytical framework not only ensures the optimization of fault feature extraction across both gear and bearing components within complex fault signals but also demonstrates remarkable efficacy in suppressing noise interference.

3.2. Wavelet packet multi-scale optimal correlation kurtosis decomposition and reconstruction

Building upon the foundational principles of the traditional Wavelet Transform (WT), the Wavelet Packet Transform (WPT) [32] represents a significant advancement in signal processing methodology, particularly in its enhanced capacity for comprehensive

frequency band decomposition. In contrast to its predecessor, the Discrete Wavelet Transform (DWT) [33], which primarily focuses on low-frequency analysis, WPT distinguishes itself through its sophisticated capability to perform both low and high-frequency decomposition, thereby achieving superior frequency resolution across the entire spectrum. This comprehensive analytical approach proves especially advantageous in the processing of non-stationary and complex signals, thus establishing itself as an indispensable tool in advanced signal analysis applications. Within this mathematical framework, when examining a discrete-time signal $y(t)$, its j-level wavelet packet decomposition, denoted as $c_k(t)$, can be systematically computed through the following mathematical formulation:

$$y(t) = \sum_{k=0}^{2^j-1} c_k(t) \tag{12}$$

$$c_k(t) = \sum_{n=0}^{N/2^j-1} x(n) \cdot h_k(n - 2^j t) \tag{13}$$

where $c_k(t)$ is the wavelet packet subband coefficient, and $h_k(n)$ denotes the wavelet basis function, which serves to extract signal characteristics across different frequency subbands. The parameter n corresponds to the signal length, while j indicates the decomposition layer count, and k represents the subband index ranging from 0 to $2^j - 1$.

The comprehensive nature of WPT enables further subdivision of each subband into smaller frequency intervals, generating multi-level coefficients of detail and approximation. This process is mathematically expressed as:

$$c_k(t) = cA_{j+1}(t) + cD_{j+1}(t) \tag{14}$$

$$cA_{j+1}(t) = \sum_{n=0}^{N/2^{j+1}-1} a_n \cdot \psi_{j+1,n}(t) \tag{15}$$

$$cD_{j+1}(t) = \sum_{n=0}^{N/2^{j+1}-1} d_n \cdot \phi_{j+1,n}(t) \tag{16}$$

where a_n is the weight of the approximation coefficient, and d_n is the weight of the detail coefficient. The scale function is represented by $\psi(t)$, whose core function is to extract low-frequency stationary components from the signal. Conversely, $\phi(t)$ serves as the wavelet basis function, specifically designed to capture high-frequency components associated with fault characteristics such as shock and noise, thereby exhibiting enhanced sensitivity to device anomalies.

The optimization of sub-zone selection for reconstruction necessitates a robust evaluation methodology. Therefore, the correlation kurtosis CK [23] serves as a quantitative measure for assessing fault characteristic strength within each detail coefficient sub-zone. This metric is mathematically defined as:

$$\mathrm{CK} = \frac{\left(\sum_{i=0}^{N-1} y(i) \cdot y(i+T)\right)^2}{\sum_{i=0}^{N-1} y(i)^2 \cdot \sum_{i=0}^{N-1} y(i+T)^2} \tag{17}$$

where T is the fault characteristic period, determined according to the required fault type. The CK values exhibits a direct relationship with the periodic shock component intensity within the signal. Through comparative analysis of maximized CK values across different level coefficients, one can effectively identify and isolate the most prominent fault signatures within the subband signal.

To establish a standardized comparison framework, the correlation kurtosis CK values undergo normalization and scaling across all subbands, yielding the weight parameter w. This normalization process serves two critical functions: eliminating magnitude disparities between subbands and quantifying the relative contribution of each subband to fault characteristics. The mathematical representation of this process follows:

$$w_k = \frac{\mathrm{CK}_k}{\sum_{i=0}^{2^j-1} \mathrm{CK}_i} \tag{18}$$

$$Y_k(f) = \mathrm{FFT}(y_k(t)) \tag{19}$$

where $\mathrm{FFT}(\cdot)$ stands for Fast Fourier Operation, and f is the frequency variable.

The subsequent signal processing phase involves extending the subband signal length from N_k to match the original signal length N through frequency-domain zero padding. This technique preserves both amplitude and phase information while maintaining signal integrity. The process employs the Inverse Fast Fourier Transform (IFFT) to generate the interpolated subband signal, ensuring minimal distortion. The mathematical framework for this operation is expressed as:

$$Y_k'(f) = \begin{cases} Y_k(f), & \text{if } |f| \le \frac{N_k}{2} \\ 0, & \text{otherwise} \end{cases} \tag{20}$$

$$y_k'(t) = \mathrm{IFFT}(Y_k'(f)) \tag{21}$$

$$y_{\text{reconstructed}}(t) = \sum_{k \in \text{topCK}} w_k \cdot y_k'(t) \tag{22}$$

The implementation of zero-padding operations serves a crucial role in maintaining signal integrity throughout the interpolation process. This technique proves particularly effective for high-frequency components, enhancing both frequency point density and

resolution. Furthermore, the incorporation of multiple subbands in the reconstruction process significantly prevents aliasing artifacts inherent in single-band processing. This approach demonstrates particular effectiveness when fault signatures manifest across various frequency ranges, as the integration of multi-subband information substantially enhances the robustness and reliability of the reconstructed signal.

3.3. Selection of periodic dynamic windows

In the domain of rotating machinery diagnostics, precise detection of periodic fault pulses in bearings and gears requires a sophisticated windowing approach. The methodology employs a dynamic sliding window mechanism that synchronizes with the characteristic failure frequency cycle, ensuring optimal fault pulse capture and analysis accuracy. The fundamental window initialization process is mathematically expressed as:

$$T = \frac{f_s}{f_c}, N_w = \left\lfloor \frac{f_s \cdot t}{T} \right\rfloor \tag{23}$$

where T represents the window size, while f_c denotes the characteristic fault frequency. The parameter N_w indicates the total number of windows, and $\lfloor \cdot \rfloor$ signifies the floor function for rounding down to the nearest integer.

The implementation employs non-overlapping sliding windows, with each subsequent window initiating immediately after the conclusion of its predecessor. The sequential placement of these windows is mathematically formalized by the window indexing equation, as specified below:

$$s_i = (i-1) \times T + 1, \quad e_i = i \times T \tag{24}$$

where s_i and e_i respectively represent the starting and ending indices of the i-th window. Within each window, the methodology identifies and records the sample point exhibiting the maximum peak amplitude, which serves as a preliminary filter for potential fault pulses. This peak detection process is formally expressed as:

$$\mathrm{loc}_i = \arg \max_{j \in [s_i, e_i]} y_{\mathrm{positive}}(j) \tag{25}$$

where $y_{\mathrm{positive}}(j)$ represents the signal value at index j after preserving the positive components of the original reconstructed signal $y_{\mathrm{reconstructed}}$.

To enhance the robustness of fault detection and accommodate potential time domain offsets in real operational conditions, the methodology incorporates an expansion mechanism. Each identified peak position undergoes bilateral extension, slightly exceeding half the window size, thereby forming an extended analysis window. This extension is mathematically described as:

$$\begin{aligned} l_i &= \max(1, \mathrm{loc}_i - \alpha \times \frac{T}{2}), \\ r_i &= \min(f_s \cdot t, \mathrm{loc}_i + \alpha \times \frac{T}{2}) \end{aligned} \tag{26}$$

where l_i and r_i denotes the starting index and the ending index of the i-th extended window, respectively. α ($\alpha > 1$) is an expansion factor, indicating the expanded window is slightly larger than the original.

By calculating the length of the overlapping sections of adjacent extended windows, the degree of overlap can be determined, allowing for the evaluation of missed detections. If the overlap length is greater than or equal to $T/3$, it is considered that no missed detection has occurred. Otherwise, it indicates a potential missed detection, necessitating additional peak detection in the overlapping area. This area is then added to the window list as a new window to ensure all significant fault pulses are captured. This important step is as follows:

$$L_{\mathrm{overlap}_i} = \min(r_i, r_{i+1}) - \max(l_i, l_{i+1}) + 1 \tag{27}$$

$$W_{\mathrm{new}} = \begin{cases} \emptyset, & \text{if } L_{\mathrm{overlap}_i} \geq \frac{T}{3} \\ \left[\max\left(l_i, l_{i+1}\right), \min\left(r_i, r_{i+1}\right)\right], & \text{if } L_{\mathrm{overlap_i}} < \frac{T}{3} \end{cases} \tag{28}$$

where L_{overlap_i} quantifies the overlap extent, while W_{new} represents potentially new windows requiring additional analysis. When $W_{\mathrm{new}} \neq \emptyset$, supplementary peak detection is performed and integrated into the existing window sequence. Conversely, the absence of overlap suggests non-periodic components, triggering a re-extraction process within the original window parameters and marking it accordingly in the updated window set.

3.4. Vibration amplitude-based grading and weighting distribution

For specific time intervals referred to as normal windows, the amplitude of the waveform in the time domain is categorized into distinct levels. This grading is based on the peak amplitude $y_{\mathrm{positive}}(\mathrm{loc})$, as depicted in Fig. 2. In this framework, dotted lines act as level boundaries, and each sampling point is assigned to the corresponding level determined by the interval it falls within. The

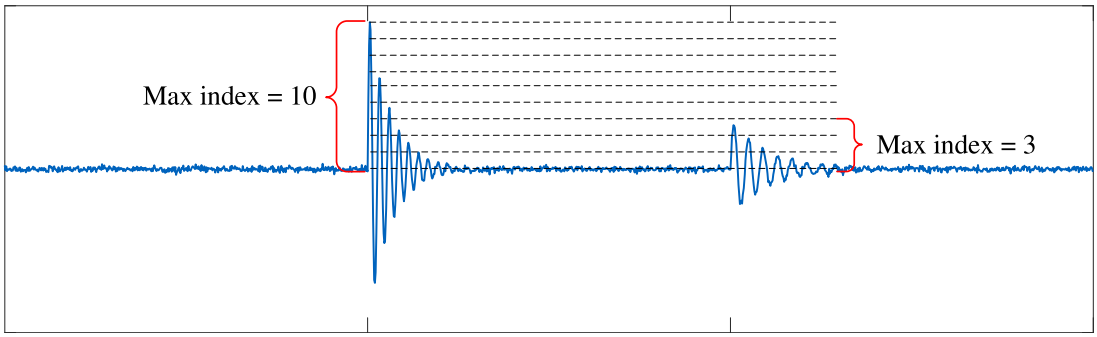

Fig. 2. Diagram of the method for vibration weighted grading index.

formula for setting the grading distribution is as follows:

$$\begin{aligned} \text{level}(j) &= \left\lfloor \frac{y_{\text{positive}}(j)}{\Delta y} \right\rfloor + 1, \\ \Delta y &= \frac{y_{\text{positive}}(\text{loc})}{n} \quad (j = 1, 2, \ldots, n) \end{aligned} \tag{29}$$

For special windows, the grading distribution is still based on the maximum peak value, but the interval is defined by the re-extracted peak value $y_{\text{positive}}(\text{loc}')$.

$$\begin{aligned} \text{level}(j) &= \left\lfloor \frac{y_{\text{positive}}(j)}{\Delta y'} \right\rfloor + 1, \\ \Delta y' &= \frac{y_{\text{positive}}(\text{loc}')}{n} \quad \left(j = 1, 2, \ldots, \left\lceil \frac{y_{\text{positive}}(\text{loc})}{\Delta y'} \right\rceil \right) \end{aligned} \tag{30}$$

where, Δy represents the distrubition interval, $\lceil \cdot \rceil$ represents the rounding up operation.

Each sampling point within these defined levels is then assigned a specific weight ω_{level}, with subsequent adjustments applied to its amplitude. This process enables the amplification of key pulse characteristics. Within normal windows, the assignment of weights ensures that lower levels receive smaller weights, while upper levels are emphasized with comparatively larger ones. Similarly, in special windows, sampling points surpassing n levels are uniformly assigned lower weights. The mathematical representation of this process is:

$$\omega_{\text{level}} = \max\left(0, 2 - \tanh\left(a_1 \frac{\text{level}}{n/2}\right) + \tanh\left(a_2 \frac{\text{level} - n/2}{n/2}\right) - b_1 \ln\left(1 + \exp\left(b_2(\text{level} - n)\right)\right)\right) \tag{31}$$

where a_1 controls the weight transition slope of low to medium level amplitudes (level $n/2$) to slow down the low level weights and avoid excessive suppression of weak pulses in the bearings. a_2 affects the transition slope of weights for medium to high-level amplitudes (level $n/2$), causing high-level weights to rise rapidly and strengthening key strong pulse features. b_1 represents the weight attenuation amplitude of super n-level amplitudes (level n, mostly noise or abnormal interference) to avoid interfering with fault characteristics. Finally, b_2 controls the weight decay rate of the super n-level amplitude, so that the weight decays exponentially with the increase of level, quickly suppressing high-frequency noise. Through cross validation, with the goal of minimizing the mean square error (MSE) between the reconstructed signal and the real fault signal, the optimal parameter combination was determined by selecting the default values of a_1, a_2, b_1, and b_2 as (2, 8, 5, 10). The effects of these parameters on the weights are illustrated in Fig. 3. Through this framework, the cumulative weight values maintain a uniform decline within the range spanning 0 to $n/2$ for standard cases, and from n to the maximum level $\left\lceil \frac{y_{\text{positive}}(\text{loc})}{\Delta y'} \right\rceil$ in special scenarios. This ensures the preservation of the attenuation

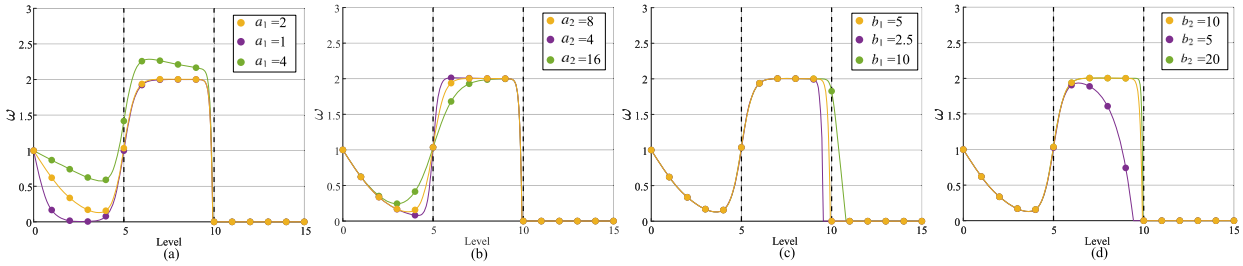

Fig. 3. Diagram of the influence of parameters on vibration-weighted grading weights

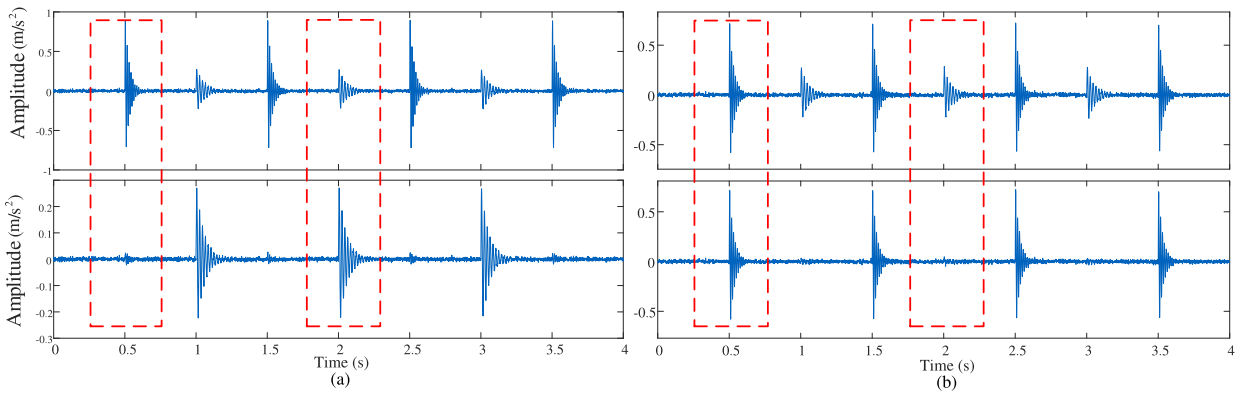

Fig. 4. Diagram of enhanced effects of weighted grading for different vibrations.

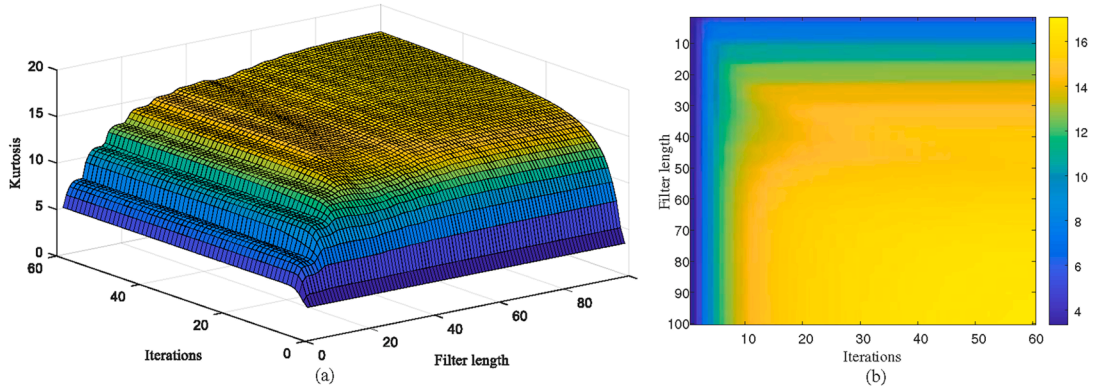

Fig. 5. (a) The 3D heatmap of the influence of different parameters on the optimal kurtosis of the MED method for single-fault signal, (b) The heatmap of the optimal kurtosis of single-fault signal under different parameters of the MED method.

form while enhancing the targeted shock peaks between levels $n/2$ and n. An example of how this adjustment modifies the impact characteristics of the waveform is presented in Fig. 4.

Finally, signals from all adjusted windows are merged into a unified dataset. During this integration, particular attention is given to sampling points associated with peak amplitudes that surpass the level $n/2$. These significant points are consolidated based on their peak values, enabling an accurate representation of critical structures while ensuring coherence across the combined signals Algorithm 1.

4. Experimental validation and comparative analysis

In this section, the discussion commences with a comprehensive analysis of filtering strategies and parameter tuning aimed at achieving optimal performance, as detailed in Section 4.1. Subsequently, the narrative progresses to the examination of two distinct case studies, presented in Section 4.2 and Section 4.3, which serve as empirical validations of the efficacy of the proposed optimized MCKD (Maximum Correlated Kurtosis Deconvolution) framework. This framework incorporates a vibration-weighted grading distribution alongside latent cyclic pattern discovery, thereby enhancing the robustness and applicability of the model in real-world scenarios. Through this structured approach, the section not only elucidates the theoretical underpinnings of the optimization techniques but also substantiates their practical utility, offering a holistic perspective on the advancements made in the field.

4.1. Analysis of filtering strategies and parameter tuning for optimal performance

This section analyzes the impact of MED filter length and different complex operating conditions on filtering performance. The operational efficacy of the MED process is fundamentally contingent upon several critical parameters, with filter length, iteration frequency, and convergence criteria emerging as particularly significant determinants. Among these interdependent variables, filter length assumes paramount importance in signal enhancement, given its substantial and variable impact on the extraction of vibration features across diverse signal characteristics. This relationship is empirically demonstrated in Fig. 5, wherein the analysis of low-noise periodic vibration signals reveals a distinctive pattern: the optimal kurtosis exhibits an initial sharp ascension before stabilizing at a plateau phase. Notably, this behavioral pattern manifests differently across varying filter lengths, whereby shorter filter configurations

Algorithm 1 An optimized MCKD framework with vibration weighted grading distribution and latent cyclic pattern discovery.

Phase I: Adaptive MED filter optimization via SN-SES

Input: Raw signal $x(t)$, f_m (gear meshing freq), BPF (bearing race freq)

Define $\Delta f^{\text{gear}} = [1, nf_m]$, $L_g = [20:5:200]$. $\Delta f^{\text{bearing}} = [1, nBPF]$, $L_b = [2:1:50]$
for $L \in \{L_g, L_b\}$ **do**
  $y_L(t) = \text{MED}(x(t) \text{ or } r(t), L)$ ▷ Gear: $x(t)$. Bearing: $r(t) = x - y_{\text{best}}^{\text{gear}}$
  $\Delta I_E = \text{SN-SES}(y_L(t), f_s, \Delta f^{\text{gear/bearing}})$ ▷ Eq. (8)
end for
$L_{\text{best}} = \arg\max(\Delta I_E)$
$y_{\text{best}} = \text{MED}(x(t) \text{ or } r(t), L_{\text{best}})$

Output: Enhanced gear $y_{\text{best}}^{\text{gear}}(t)$ and bearing $y_{\text{best}}^{\text{bearing}}(t)$ **Phase II: Wavelet packet decomposition with correlation kurtosis**

Input: $y_{\text{best}}^{\text{gear}}(t)$, $y_{\text{best}}^{\text{bearing}}(t)$

for each enhanced signal $y(t)$ **do**
  Perform j-level wavelet packet decomposition: $y(t) = \sum c_k(t)$ ▷ Eq. (22)
  Compute $CK_k = \text{CorrKurt}(c_k(t))$ ▷ Eq. (17)
  $w_k = CK_k / \sum CK_i$ ▷ Eq. (18)
  Select top subbands, interpolate via $Y_k'(f) = \text{ZeroPadding}(\text{FFT}(c_k), N)$ ▷ Eq. (20)
  $y_{\text{rec}}(t) = \sum w_k \cdot \text{IFFT}(Y_k'(f))$ ▷ Eq. (21)–(22)
end for

Output: Reconstructed signals $y_{\text{rec}}^{\text{gear}}(t)$, $y_{\text{rec}}^{\text{bearing}}(t)$ **Phase III: Periodic dynamic window selection**

Input: $y_{\text{rec}}(t)$, $f_c \in \{f_m, BPF\}$

$T = f_s/f_c$, $N_w = \lfloor f_s \cdot t/T \rfloor$ ▷ Eq. (23)
Define windows: $s_i = (i-1)T + 1$, $e_i = iT$
Find peaks: $\text{loc}_i = \arg\max_{[s_i, e_i]} y_{\text{positive}}$ ▷ Eq. (24)–(25)
Extend windows: $l_i = \max(1, \text{loc}_i - \alpha T/2)$, $r_i = \min(f_s t, \text{loc}_i + \alpha T/2)$ ▷ Eq. (26)
Check overlap: $L_{\text{overlap}_i} = \min(r_i, r_{i+1}) - \max(l_i, l_{i+1}) + 1$
Add W_{new} if $L_{\text{overlap}_i} < T/3$

Output: Window params $\{s_i, e_i, \text{loc}_i\}$, W_{new} **Phase IV: Vibration weight grading**

Input: Window params, $y_{\text{rec}}(t)$

for normal windows **do**
  $\Delta y = y_{\text{positive}}(\text{loc}_i)/n$
  $\text{level}(j) = \lfloor y_{\text{positive}}(j)/\Delta y \rfloor + 1$ ▷ Eq. (29)
end for
for special windows in W_{new} **do**
  $\Delta y' = y_{\text{positive}}(\text{loc}')/n$
  $\text{level}(j) = \lfloor y_{\text{positive}}(j)/\Delta y' \rfloor + 1$ ▷ Eq. (30)
end for
$\omega_{\text{level}} = \max(0, 2 - \tanh(a_1 \cdot \text{level}/(n/2)) + \tanh(a_2 \cdot (\text{level} - n/2)/(n/2)) - b_1 \ln(1 + \exp(b_2(\text{level} - n))))$ ▷ Eq. (31)
$y_{\text{weighted}} = y_{\text{rec}} \cdot \omega_{\text{level}}$

Output: Weight-graded signals $y_{\text{wg}}^{\text{gear}}(t)$, $y_{\text{wb}}^{\text{bearing}}(t)$

generate characteristic stepped patterns, while extended filter lengths facilitate the achievement of a more stable and uniform state in periodic signal enhancement.

In the pursuit of comprehensive understanding regarding filter length optimization, an extensive analysis was systematically conducted across multiple composite fault signals, each encompassing distinct characteristic components. The empirical findings, meticulously documented and visualized in Fig. 6, elucidate the intricate relationship between filter length configurations and their consequent impact on signal enhancement efficacy. Notably, when implementing larger filter lengths, the methodology exhibited a consistent pattern of preferentially amplifying high-amplitude periodic impulses while simultaneously attenuating impulses of lesser magnitude. In contrast, the application of smaller filter lengths yielded an inverse effect, manifesting in enhanced low-amplitude impulses and elevated noise levels, albeit at the expense of subdued high-amplitude impulse amplification. A particularly significant observation emerged regarding the temporal spacing between distinct impulses, which demonstrated minimal influence on the ultimate filtering outcomes. Furthermore, upon the filter length transcending the transition state–as evidenced in the heatmap analysis–and progressing into the steady-state domain, the variability in filtering results diminishes substantially. Consequently, this empirical evidence suggests that the optimal filter length determination can be strategically approached by leveraging the stepped transition states of optimal kurtosis, thereby achieving an ideal equilibrium between analytical precision and methodological robustness.

The complexity of filter length selection assumes heightened significance in contexts where vibration signals are subjected to contamination by transient non-Gaussian noise, introducing additional layers of analytical challenges. In particularly challenging

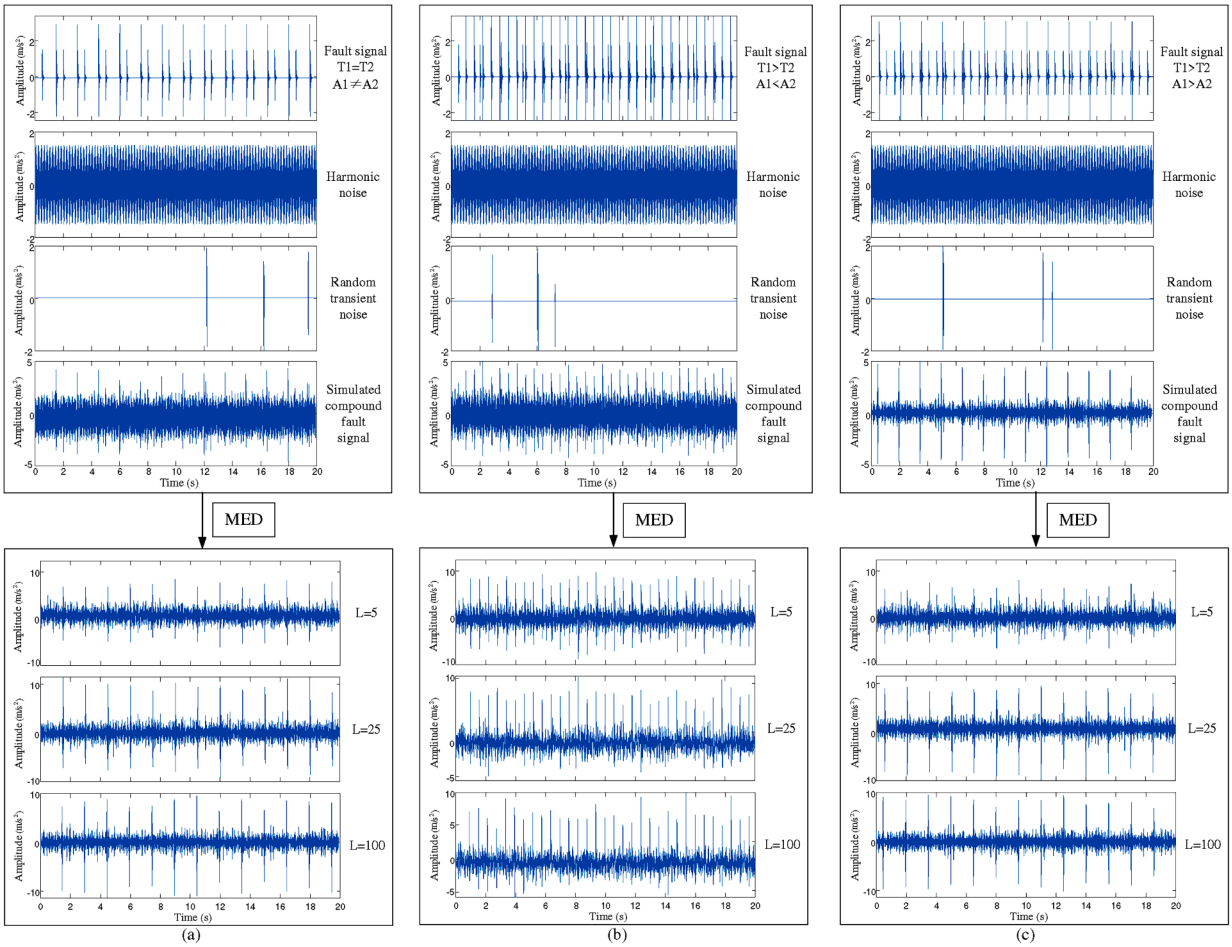

Fig. 6. The filtering effect of different filter lengths of MED method on various compound faults: (a) Impulses with different amplitudes and same intervals, (b) Impulses with larger amplitudes and smaller intervals, impulses with smaller amplitudes and larger intervals, (c) Impulses with larger amplitudes and larger intervals, impulses with smaller amplitudes and smaller intervals.

scenarios, the iterative processes inherent to the MED methodology may generate anomalously elevated kurtosis values in response to noise interference, subsequently manifesting as disorganized, non-stationary filtering patterns within the heatmap visualization, as comprehensively illustrated in Fig. 7. These aberrant outcomes frequently materialize when the selected filter length inadvertently corresponds with high-kurtosis noise components, thereby emphasizing the critical importance of circumventing such problematic length selections through meticulous parameter optimization. This consideration assumes particular relevance in the analysis of signals associated with bearing and gear degradation patterns, where the presence of transient noise can significantly obscure crucial fault characteristics. Through the strategic implementation of carefully calibrated filter lengths that systematically avoid these anomalous conditions, the deleterious effects of noise interference can be substantially minimized, thereby enhancing both the reliability and precision of fault diagnostic procedures in practical applications. Moreover, this refined approach facilitates more robust signal processing outcomes, particularly in environments characterized by complex noise profiles and multiple fault signatures.

4.2. Case study I

In the pursuit of advancing mechanical system diagnostics and fault detection methodologies, this research presents a meticulously compiled gearbox dataset, acquired through high-precision measurements of a sophisticated gear transmission system. The data presented in this case study were gathered from an experimental platform specifically engineered for fault simulation of subway train bogies, as illustrated in Fig. 8. This sophisticated platform has been carefully designed and calibrated to replicate the structural and operational characteristics of actual subway train bogies, maintaining a precise scale ratio of 1:2 relative to the real bogie. Comprising a single transmission chain, the setup integrates essential components such as a motor, a gearbox, and two axle boxes, with the entire chain powered by a three-phase asynchronous AC motor, while the load is systematically applied through electro-hydraulic loading equipment. Key specifications include the use of SKF 6205-2RSH bearings for the motor, helical gears within the reduction gearbox featuring 16 teeth on the driving gear and 107 on the driven gear, HRB 32,305 bearings for the axial support of the driving gear,

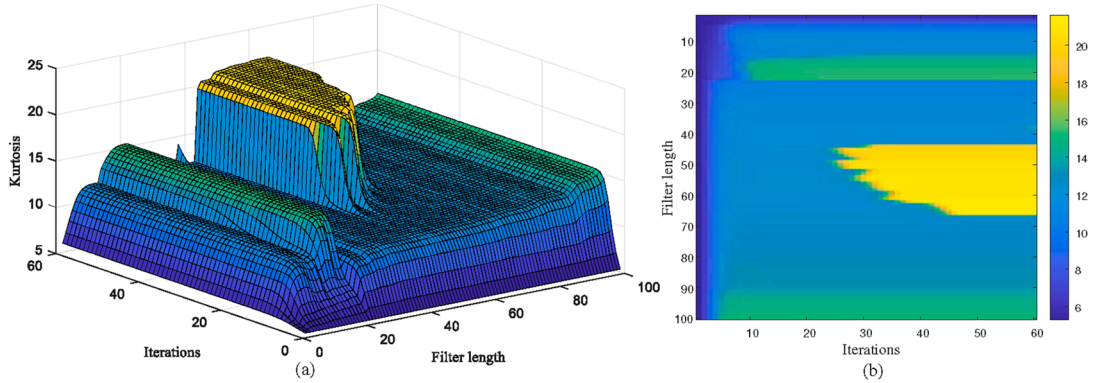

Fig. 7. (a) The 3D heatmap of the influence of different parameters on the optimal kurtosis of the MED method for single-fault signal with transient noise, (b) The heatmap of the optimal kurtosis of single-fault signal with transient noise under different parameters of the MED method.

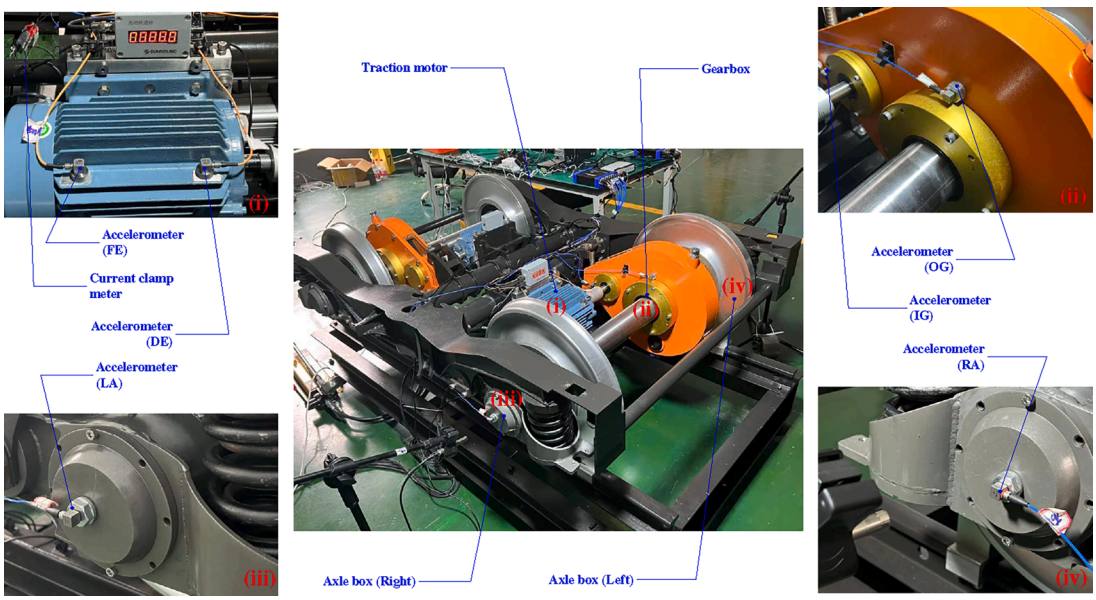

Fig. 8. Experimental setup for fault simulation in subway train transmission systems.

Fig. 9. Condition of faults in train transmission components. (a) Chipped tooth on gear. (b) Fault in bearing inner race.

and HRB 352,213 bearings for the axle boxes. During the experiments, vibration signals associated with both gearbox and bearing components under conditions of component-level compound faults–specifically, a chipped tooth on the gear and a bearing inner race fault, as detailed in Fig. 9, were diligently recorded, employing a high sampling frequency of 64 kHz to ensure detailed and accurate data capture for subsequent analysis.

Under conditions of steady rotational speed, a 1-second vibration signal, illustrated as the blue waveform in Fig. 10(b), highlights a significant diagnostic obstacle: the complex signatures of composite faults are substantially masked by an omnipresent backdrop of intense noise. Findings from the adaptive optimization of the MED filter, grounded in the spectral negentropy criterion, demonstrate

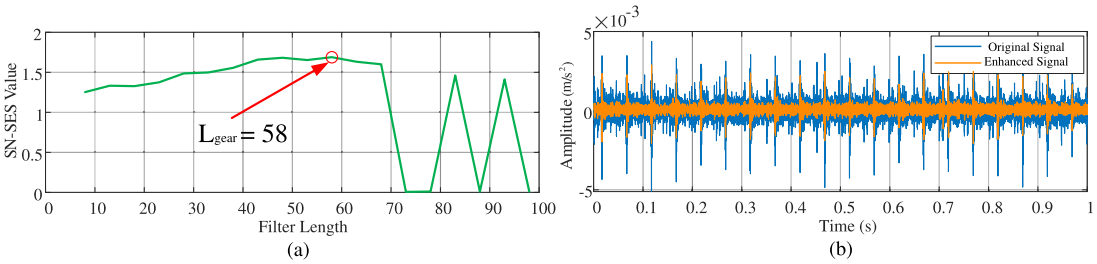

Fig. 10. (a) SN-SES of the optimal MED filter length for enhancing signal characteristics of gear fault. (b) The comparison between the original signal and the filtered signal.

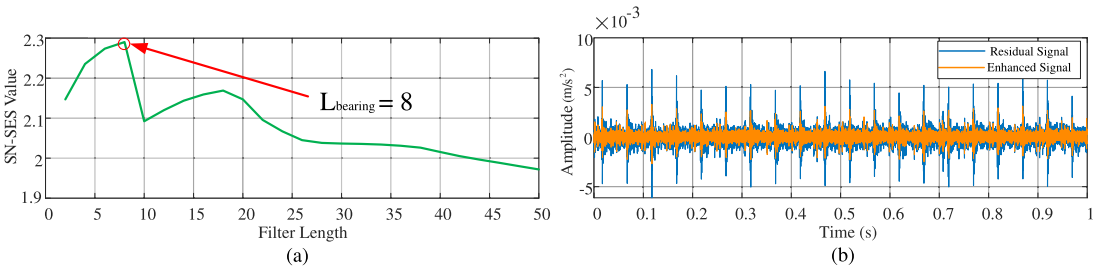

Fig. 11. (a) SN-SES of the optimal MED filter length for enhancing signal characteristics of bearing fault. (b) The comparison between the residual signal and the filtered signal.

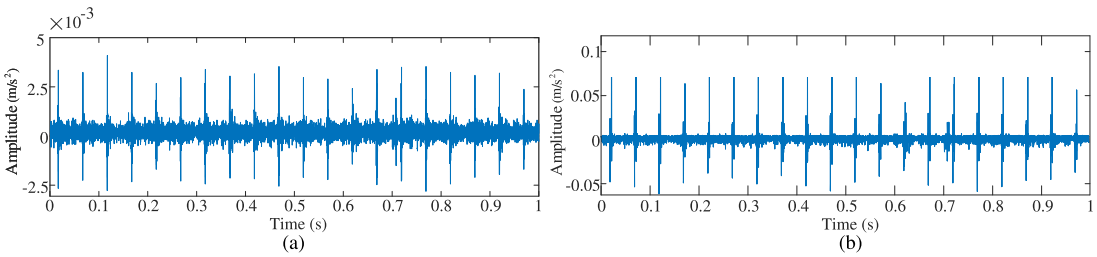

Fig. 12. (a) Reconstructed gear fault signal using Fourier interpolation following optimal correlation kurtosis decomposition of wavelet packets. (b) Obtained signal based on vibration weight grading distribution.

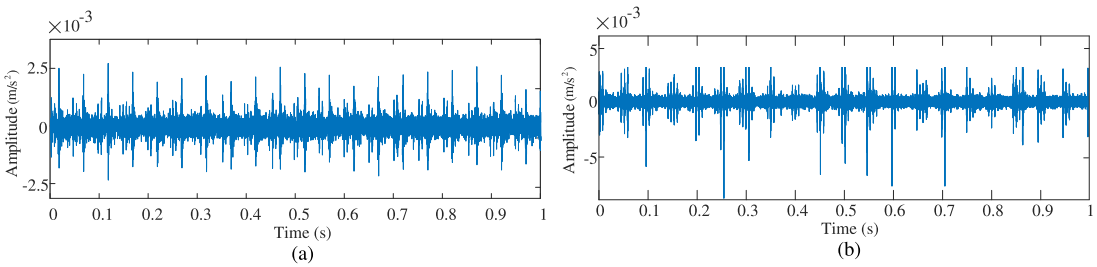

Fig. 13. (a) Reconstructed bearing fault signal utilizing Fourier interpolation after optimal correlation kurtosis decomposition of wavelet packets. (b) Obtained signal derived from vibration weight grading distribution.

that the gear fault component reaches its peak ΔI_E value at a filter length of $L = 58$, after which an oscillatory pattern emerges with increasing filter lengths, as depicted in Fig. 10(a). This meticulously selected parameter allows the post-filtered, gear-enhanced signal to manifest more distinct gear fault impact characteristics in comparison to the unprocessed signal, while concurrently mitigating signal artifacts and achieving a modest enhancement in the signal-to-noise ratio, as evidenced in Fig. 10(b). For the purpose of isolating bearing faults, a distinct parametric approach is employed. The analysis reveals that a filter length of $L = 8$ for the residual signal yields a local maximum in ΔI_E, with further increases in length resulting in a consistent decline in ΔI_E, as shown in Fig. 11(a). A comparative evaluation of the time-domain waveforms post-filtering, presented in Fig. 11(b), indicates that high-amplitude impacts attributable to gear faults are effectively attenuated, whereas the characteristic impact features of bearing inner ring faults are adeptly extracted from the surrounding noise floor, thereby facilitating precise fault identification.

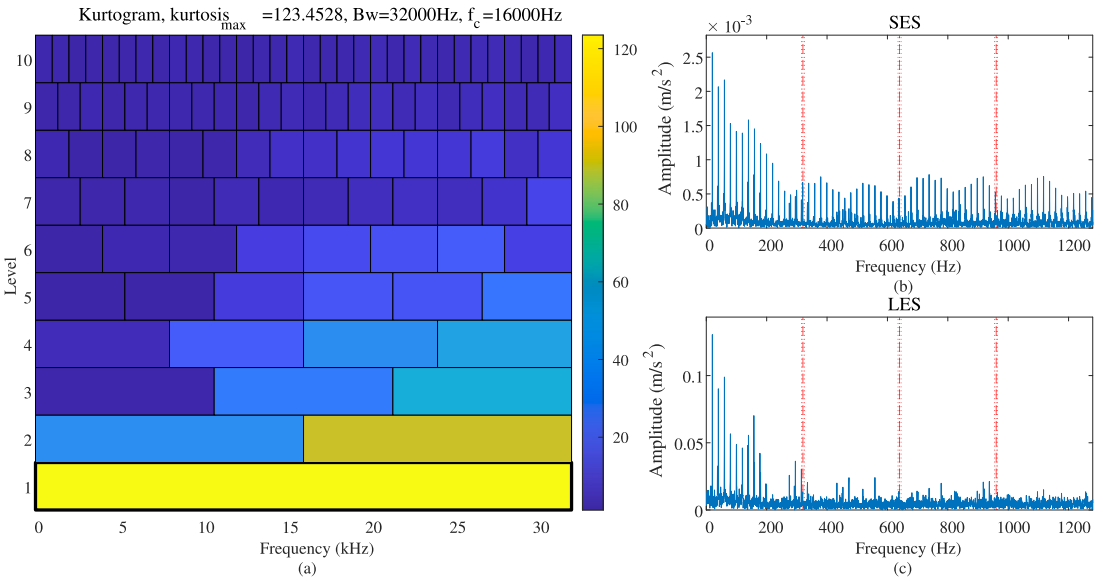

Fig. 14. Raw signal impacted by a compound fault involving both bearings and gears in Case I: (a) Demodulation band determination via Fast-Kurtogram, (b) Squared envelope spectrum analysis, (c) Logarithmic-scale envelope spectral analysis.

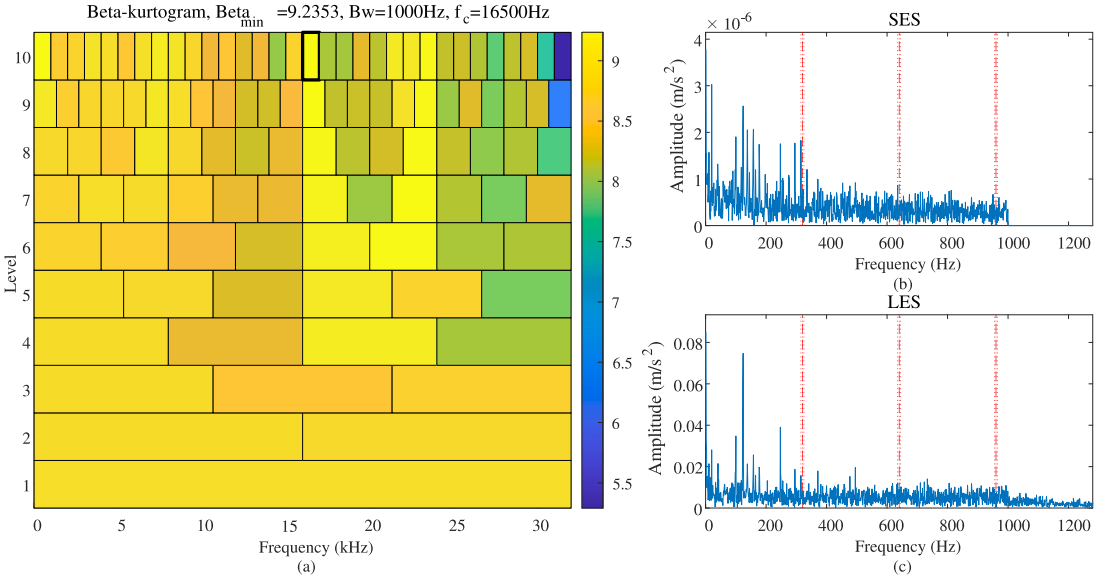

Fig. 15. Raw signal impacted by a compound fault of bearings and gears in Case I: (a) Demodulation band determination via Beta-Kurtogram, (b) Squared envelope spectrum, (c) Logarithmic scale envelope spectral analysis.

The results of processing the gear fault signal through wavelet packet multi-scale optimal correlation kurtosis decomposition and subsequent reconstruction are illustrated in Fig. 12, with Fig. 12(a) specifically illustrating the signal reconstructed using Fourier interpolation. During this intricate reconstruction process, the Correlation Kurtosis (CK) for each subband is initially computed as per Eq. (17), enabling the selective retention of subbands exhibiting elevated CK values that align with the periodic impact characteristics typical of gear meshing. Following this, by integrating weight normalization calculations from Eq. (6) with Fourier interpolation techniques outlined in Eqs. (19)-(21), the reconstructed signal ultimately reveals significantly clearer periodic impact patterns within the time domain. In comparison to the original, unprocessed signal, there is a marked enhancement in the periodic regularity of high-amplitude impact pulses, accompanied by a substantial reduction in noise interference. This improvement not only underscores the sensitivity of CK to periodic components but also highlights the efficacy of Fourier interpolation in preserving signal integrity. Following this, non-overlapping sliding windows are established according to Eq. (24). Within each window, amplitude peaks are identified using Eq. (25) to pinpoint the locations of potential fault pulses. To account for time offsets, these peaks are extended on both sides as per Eq. (26), creating analysis windows. Subsequently, an overlap analysis is conducted to add windows in areas with inadequate overlap, thereby minimizing the risk of missed detections and enhancing both the precision and reliability of fault detection. Further

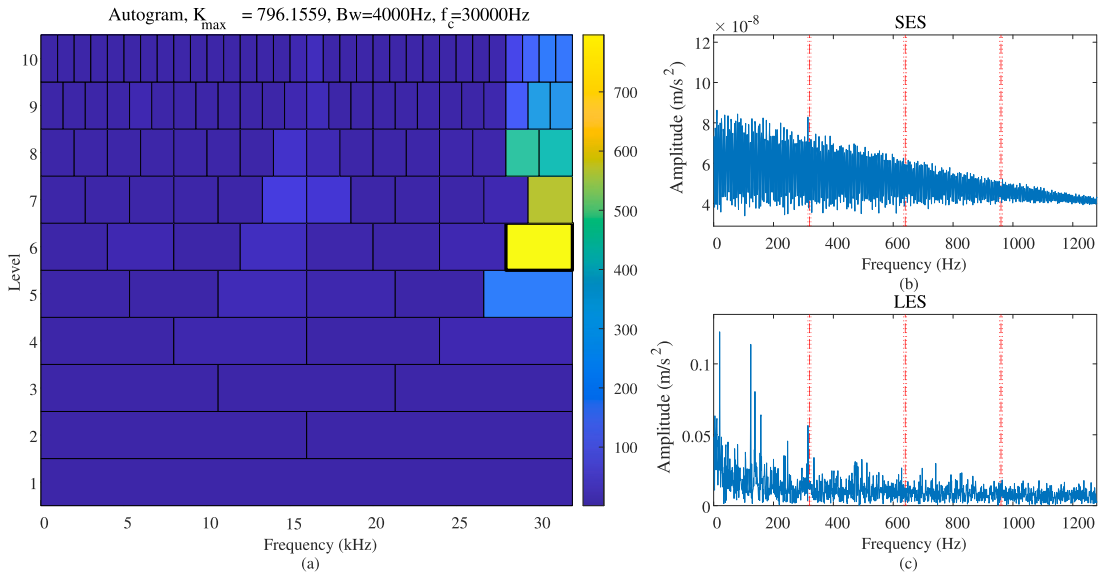

Fig. 16. Raw signal impacted by a compound fault of bearings and gears in Case I: (a) Demodulation band determination via Autogram, (b) Squared envelope spectrum, (c) Logarithmic scale envelope spectral analysis.

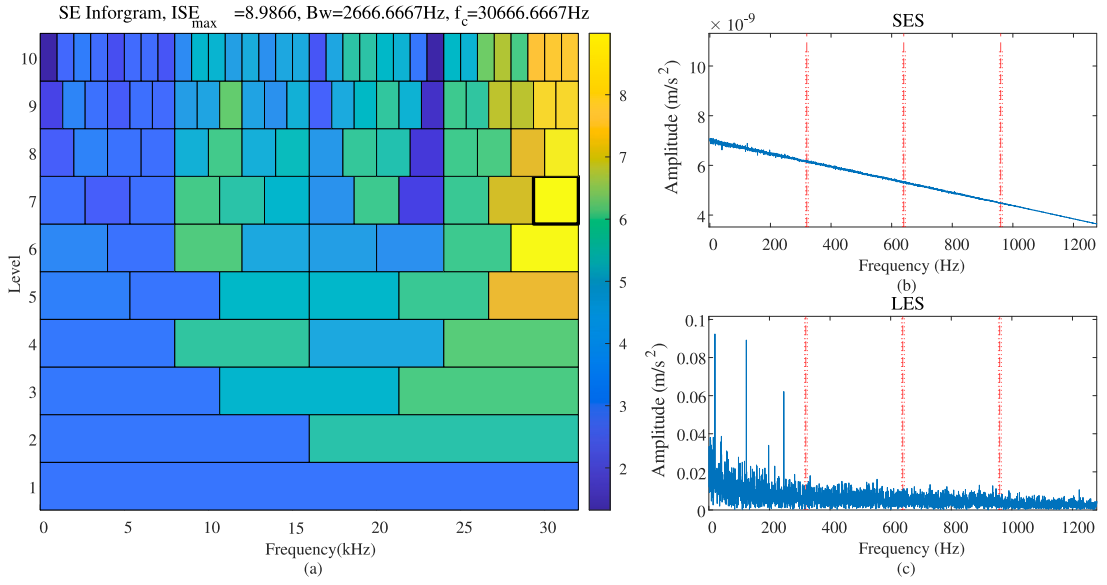

Fig. 17. Raw signal impacted by a compound fault of bearings and gears in Case I: (a) Demodulation band determination via Infogram, (b) Squared envelope spectrum, (c) Logarithmic scale envelope spectral analysis.

refinement is achieved through the vibration weight grading adjustment, as depicted in Fig. 12(b) and implemented via Eqs. (29) to (31), where Eq. (29) establishes hierarchical levels using the gear fault peak as a reference point, and the weight function in Eq. (31) amplifies high-level impacts through a sophisticated blend of hyperbolic tangent and exponential decay mechanisms while effectively attenuating low-amplitude noise. The resulting visualization clearly demonstrates a further suppression of signal noise interference, ensuring that only the impacts directly associated with gear faults are prominently enhanced.

Similarly, the processing outcomes for the bearing fault signal are presented in Fig. 13, with the reconstructed signal in Fig. 13(a) also employing wavelet packet decomposition and CK screening to target subbands with high CK values that correspond to the fault frequency of the bearing inner ring. Upon application of Fourier interpolation, the high-amplitude interference stemming from gear faults is notably diminished, thereby allowing the subtler impact characteristics of the bearing inner ring to be distinctly isolated from the background noise floor. Throughout this process, several critical mechanisms ensure precision: the periodic window initialization, as defined in Eq. (23), adapts the window size to match the bearing fault cycle. The sliding window, described in Eq. (24), efficiently captures the peak within each cycle. The extended window, detailed in Eq. (26), mitigates the risk of missed detections due to

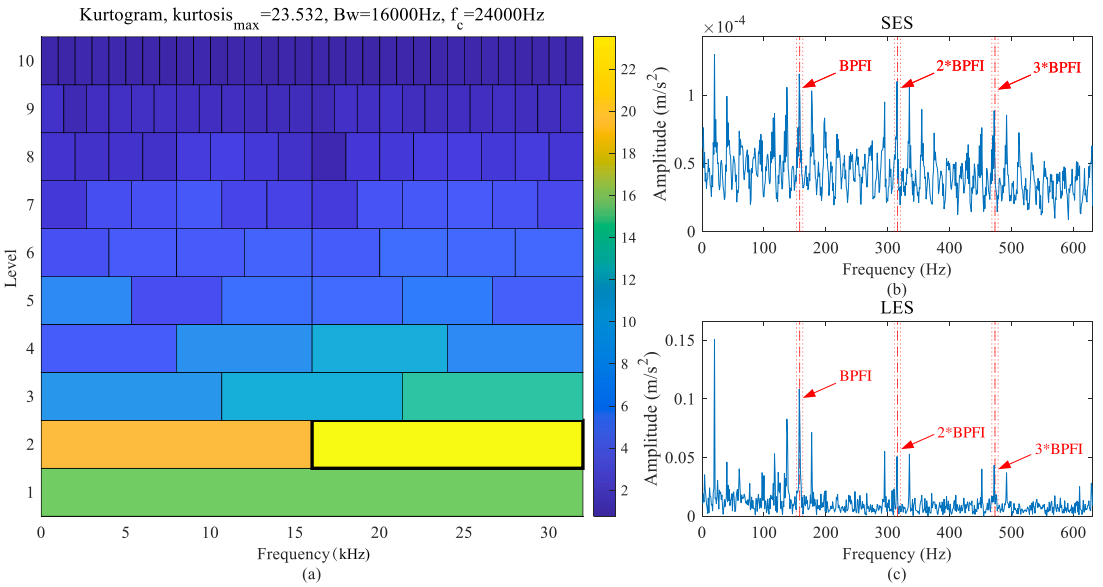

Fig. 18. Case I: (a) Demodulation band determination via Fast-Kurtogram, (b) Squared envelope spectrum, (c) Logarithmic scale envelope spectral analysis.

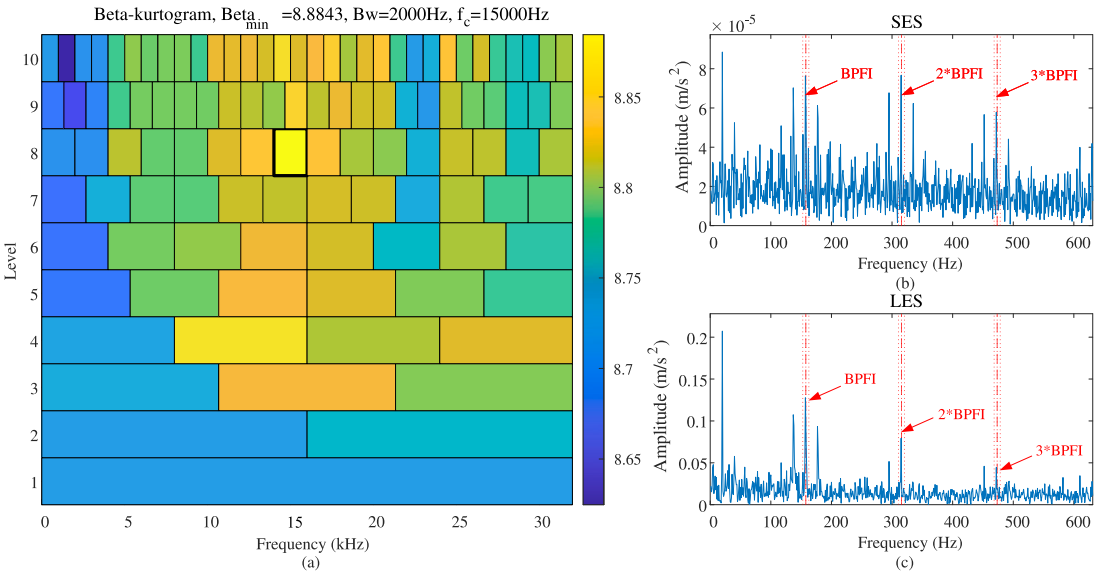

Fig. 19. Case I: (a) Demodulation band determination via Beta-Kurtogram, (b) Squared envelope spectrum, (c) Logarithmic scale envelope spectral analysis.

time-domain offsets through strategic bilateral expansion. The vibration weight grading adjusted signal, showcased in Fig. 13(b), provides compelling evidence of the method's efficacy, as gear-related impacts are constrained to near-zero levels through carefully calibrated weight settings, while the impacts associated with bearing faults are significantly amplified. Collectively, these results not only affirm the adaptability of the proposed methodology across diverse fault types but also reinforce the robustness and reliability of the reconstructed signals in diagnostic applications.

To further validate the effectiveness of the proposed fault separation framework, this study constructs a comparative analysis involving four well-established signal processing methodologies: Fast-Kurtogram, Beta-Kurtogram, Autogram, and Infogram. These techniques are methodically applied to three distinct signal categories within Case I, namely raw signals exhibiting compound bearing and gear faults, signals following the isolation of bearing faults, and signals after the separation of gear faults. The primary objective of this evaluation is to critically assess the performance of each method with respect to demodulation band selection and the extraction of fault-specific features, thereby providing a robust benchmark for the proposed framework's effectiveness in enhancing diagnostic precision.

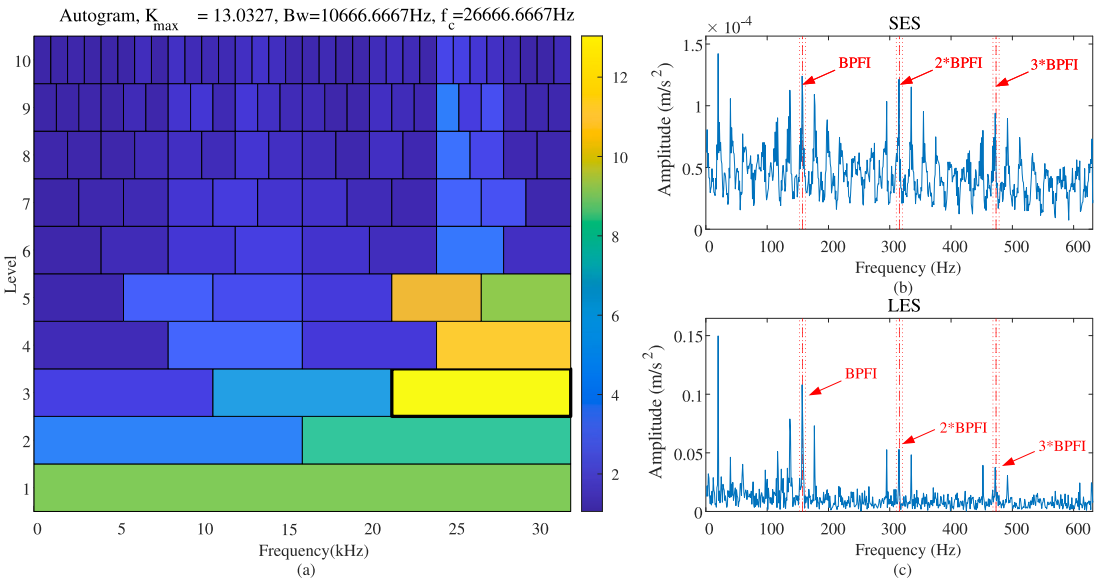

Fig. 20. Case I: (a) Demodulation band determination via Autogram, (b) Squared envelope spectrum, (c) Logarithmic scale envelope spectral analysis.

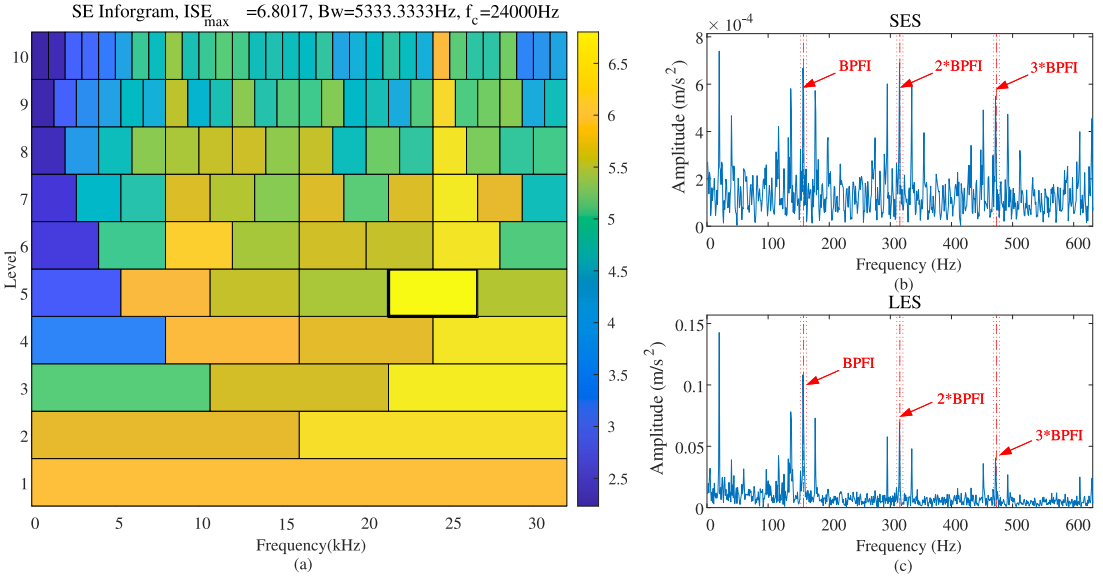

Fig. 21. Case I: (a) Demodulation band determination via Infogram, (b) Squared envelope spectrum, (c) Logarithmic scale envelope spectral analysis.

The analytical results for raw compound fault signals, as detailed in Figs. 14 through 17, consistently highlight inherent limitations across all evaluated techniques. For instance, Fast-Kurtogram, as shown in Fig. 14(a), opts for an excessively wide frequency band of [16000Hz, 32000Hz], which encapsulates the resonant regions of both fault types, consequently resulting in overlapping features in the SES (Fig. 14(b)). Here, the bearing characteristic frequency (BPFI = 159.6Hz), gear characteristic frequency (f_m = 320Hz) and sideband frequency (f_r = 20Hz) coalesce into indistinct peaks, while the LES (Fig. 14(c)) is predominantly overwhelmed by low-frequency components that obscure critical fault signatures. Similarly, although Beta-Kurtogram employs a narrower band of [16500Hz, 1000Hz] (Fig. 15(a)) to mitigate interference, it fails to capture essential harmonics in either SES (Fig. 15(b)) or LES (Fig. 15(c)). Furthermore, Autogram's high-frequency band selection of [30000Hz, 4000Hz] (Fig. 16(a)) yields noise-dominated spectra, completely masking characteristic frequencies in both SES (Fig. 16(b)) and LES (Fig. 16(c)), thus severely limiting feature recognition. In a parallel vein, Infogram's selected band of [30666.6667Hz, 2666.6667Hz] (Fig. 17(a)) proves equally ineffective in distinguishing the two fault types in either SES (Fig. 17(b)) or LES (Fig. 17(c)), underscoring the challenges inherent in processing unseparated signals.

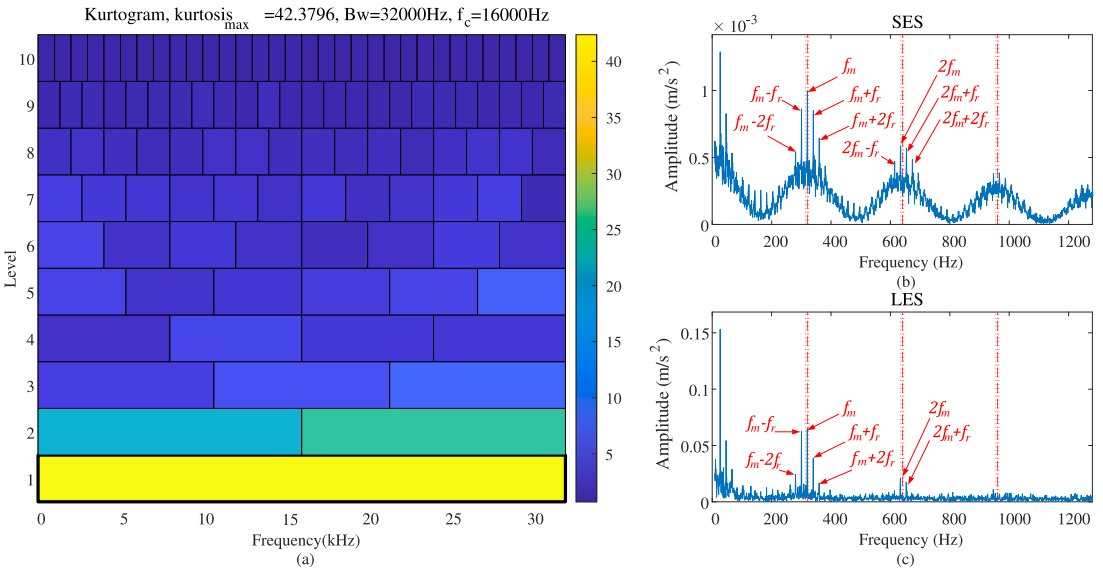

Fig. 22. Case I: (a) Demodulation band determination via Fast-Kurtogram, (b) Squared envelope spectrum, (c) Logarithmic scale envelope spectral analysis.

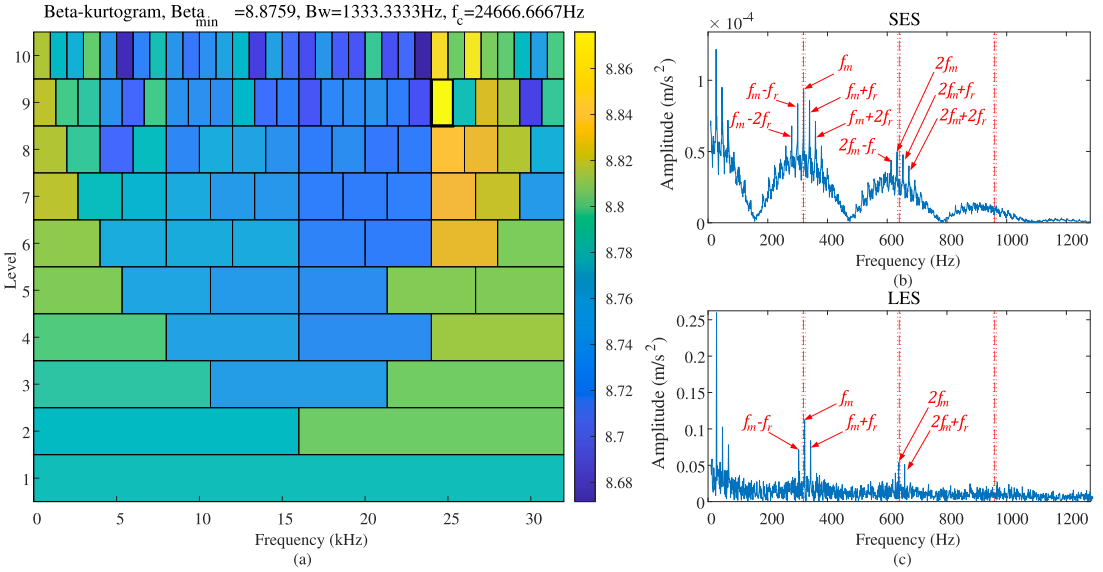

Fig. 23. Case I: (a) Demodulation band determination via Beta-Kurtogram, (b) Squared envelope spectrum, (c) Logarithmic scale envelope spectral analysis.

In contrast, the performance of these techniques exhibits a significant enhancement when applied to signals following bearing fault separation, as evidenced in Figs. 18 through 21. Fast-Kurtogram, for example, narrows its focus to a targeted band of [24000Hz, 16000Hz] (Fig. 18(a)), effectively honing in on bearing resonance and producing distinct peaks at 160Hz alongside harmonics at 320Hz and 480Hz in the SES (Fig. 18(b)), while the LES (Fig. 18(c)) displays diminished interference from the 20Hz rotational frequency, thereby improving the visibility of bearing features. Similarly, Beta-Kurtogram's refined band of [15000Hz, 2000Hz] (Fig. 19(a)) optimally encompasses bearing resonance, with SES (Fig. 19(b)) revealing sharp characteristic peaks accompanied by rotational frequency sidebands, and LES (Fig. 19(c)) achieving an exemplary signal-to-noise ratio and feature purity. In addition, Autogram's band selection of [26666Hz, 10666Hz] (Fig. 20(a)) uncovers regular distributions of 160Hz and its harmonics in SES (Fig. 20(b)), complemented by clear peaks of characteristic frequencies and their multiples in LES (Fig. 20(c)). Lastly, Infogram's chosen band of [24000Hz, 5333Hz] (Fig. 21(a)) markedly enhances peak visibility in both SES (Fig. 21(b)) and LES (Fig. 21(c)), thus providing compelling validation of the successful preservation of bearing features in signals post-separation.

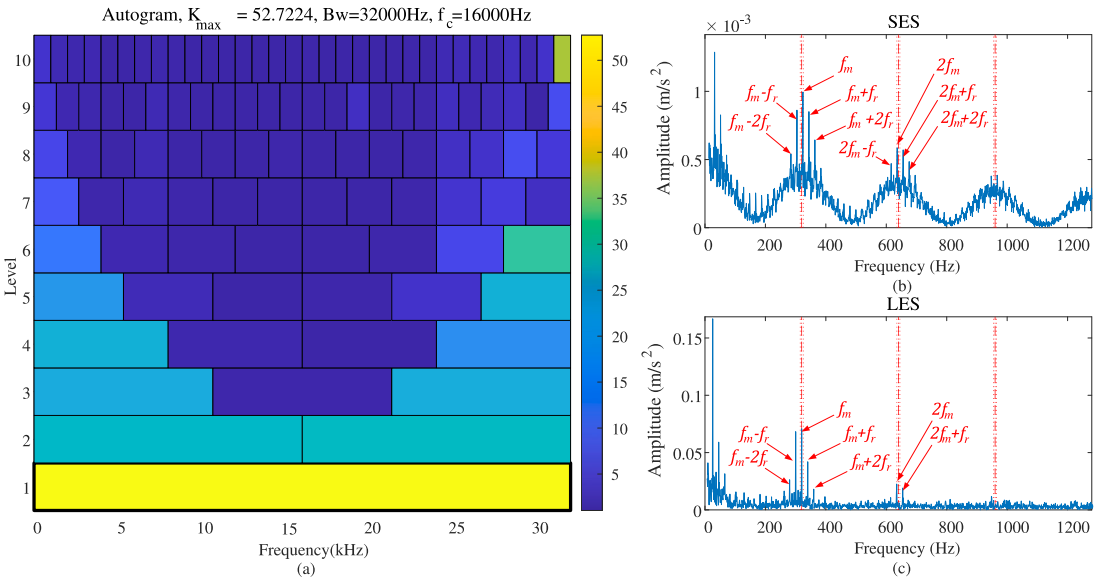

Fig. 24. Case I: (a) Demodulation band determination via Autogram, (b) Squared envelope spectrum, (c) Logarithmic scale envelope spectral analysis.

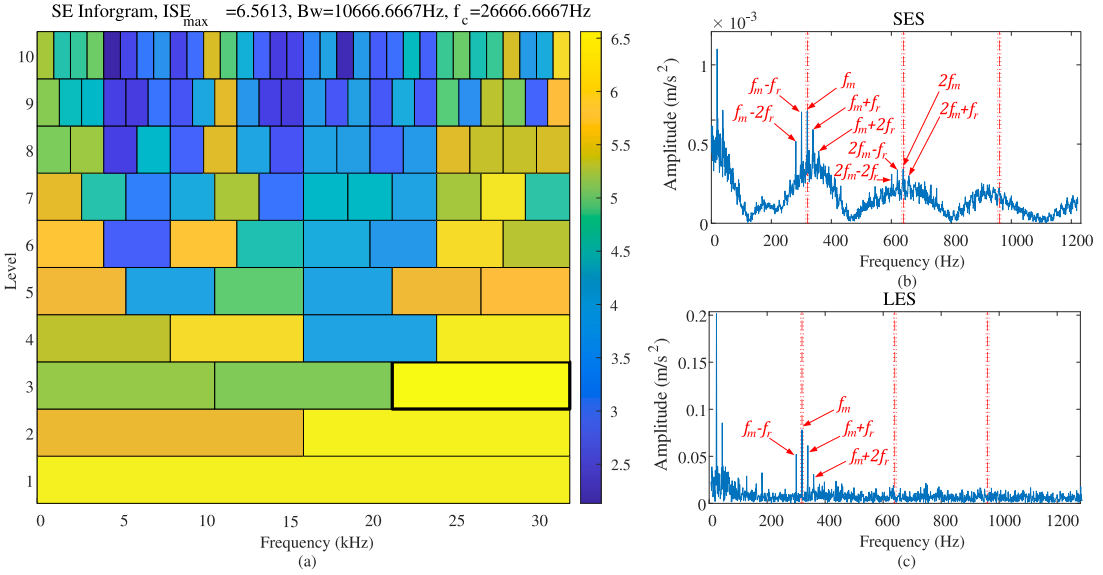

Fig. 25. Case I: (a) Demodulation band determination via Infogram, (b) Squared envelope spectrum, (c) Logarithmic scale envelope spectral analysis.

In the analysis of gear fault-separated signals, as detailed in Figs. 22 to 25, all evaluated signal processing techniques exhibit a notable improvement in performance. Specifically, Fast-Kurtogram maintains its original frequency band of [16000Hz, 32000Hz] (Fig. 22(a)). However, with bearing-related interference effectively mitigated, the SES (Fig. 22(b)) distinctly resolves the gear meshing frequency (f_m), its harmonics (2*f_m, 3*f_m), and the rotational frequency (f_r), while the LES (Fig. 22(c)) demonstrates a significant reduction in 20Hz rotational interference, thereby preserving essential fault characteristics. Similarly, Beta-Kurtogram, with its refined band of [24666Hz, 1333Hz] (Fig. 23(a)), produces an SES (Fig. 23(b)) that highlights prominent peaks at f_m and 2*f_m, and an LES (Fig. 23(c)) that presents uninterrupted fault features devoid of bearing-related disturbances. Furthermore, Autogram's band selection of [16000Hz, 32000Hz] (Fig. 24(a)) effectively captures comprehensive harmonic distributions in both SES (Fig. 24(b)) and LES (Fig. 24(c)), rendering it well-suited for multi-order gear fault analysis. Lastly, Infogram's chosen band of [26666Hz, 10666Hz] (Fig. 25(a)) reveals that, although high-order harmonics in the SES (Fig. 25(b)) possess relatively weak energy, the fundamental frequency features remain stable, and in the LES (Fig. 25(c)), even low-amplitude harmonics are distinctly discernible.

In summary, the analysis of raw signals reveals a critical limitation, as their frequency bands contain a mix of overlapping components, resulting in indistinct SES and LES features across all investigated techniques. In contrast, the application of precise band

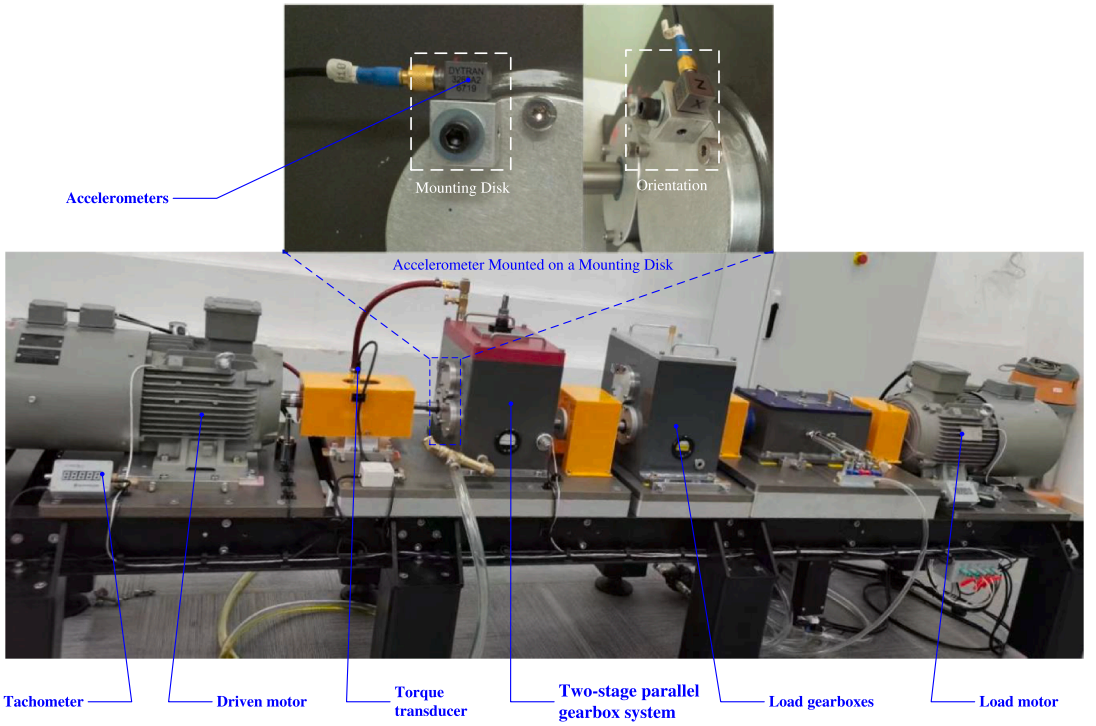

Fig. 26. The real-world test-rig of gear transmission system.

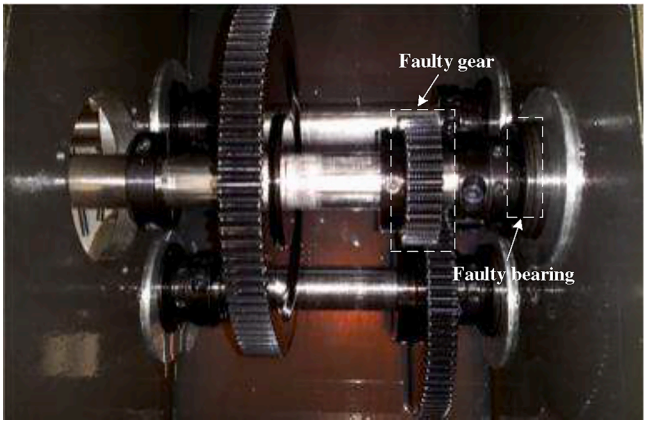

Fig. 27. The internal structure diagram of the gearbox.

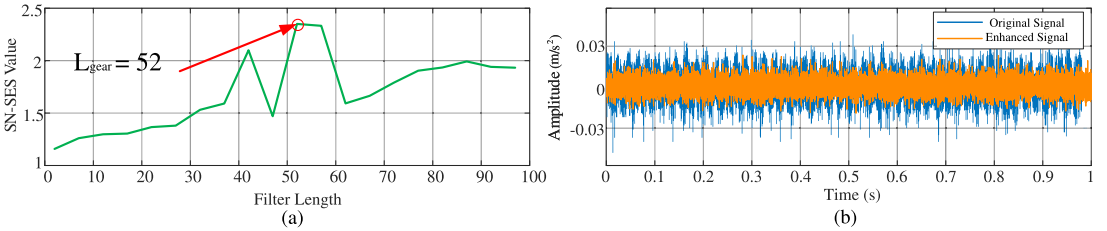

Fig. 28. (a) SN-SES of the optimal MED filter length for enhancing signal characteristics of gear fault. (b) The comparison between the original signal and the filtered signal.

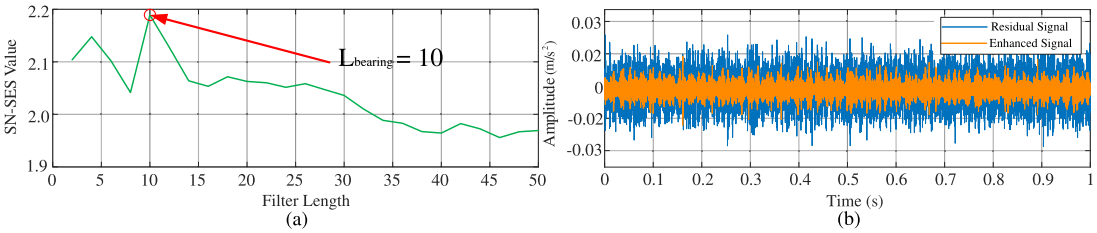

Fig. 29. (a) SN-SES of the optimal MED filter length for enhancing signal characteristics of bearing fault. (b) The comparison between the residual signal and the filtered signal.

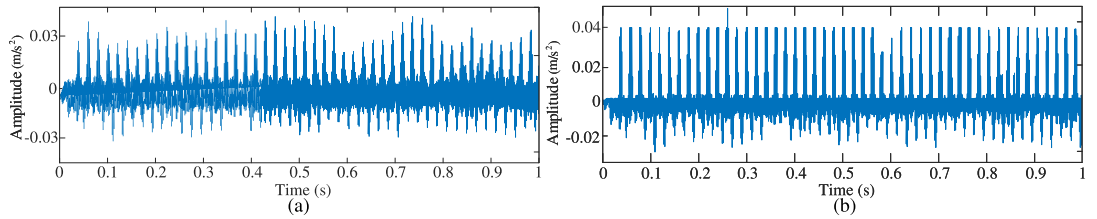

Fig. 30. (a) Gear fault signal reconstructed by Fourier interpolation after the optimal correlation kurtosis decomposition of wavelet packets. (b) Vibration weight grading distribution adjusted signal.

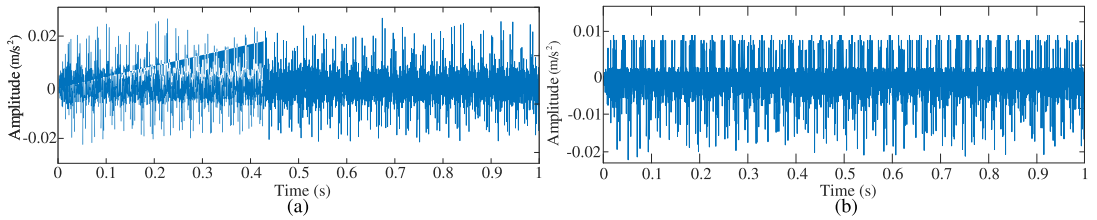

Fig. 31. (a) Bearing fault signal reconstructed by Fourier interpolation after the optimal correlation kurtosis decomposition of wavelet packets. (b) Vibration weight grading distribution adjusted signal.

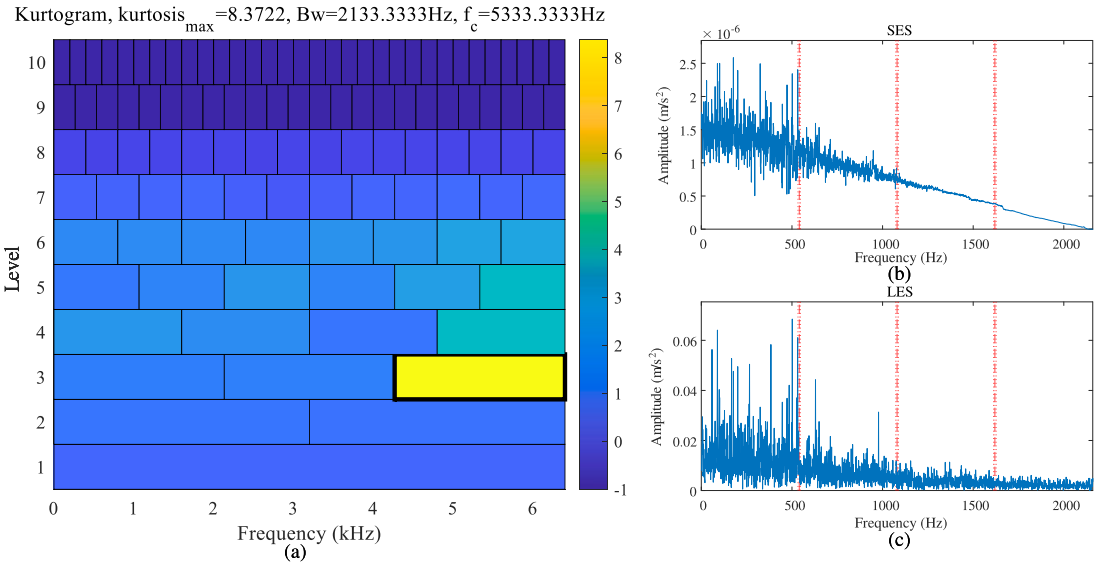

Fig. 32. Raw signal affected by a compound fault of bearings and gears. in Case II: (a) Demodulation band determination via Fast-Kurtogram, (b) Squared envelope spectrum, (c) Logarithmic scale envelope spectral analysis.

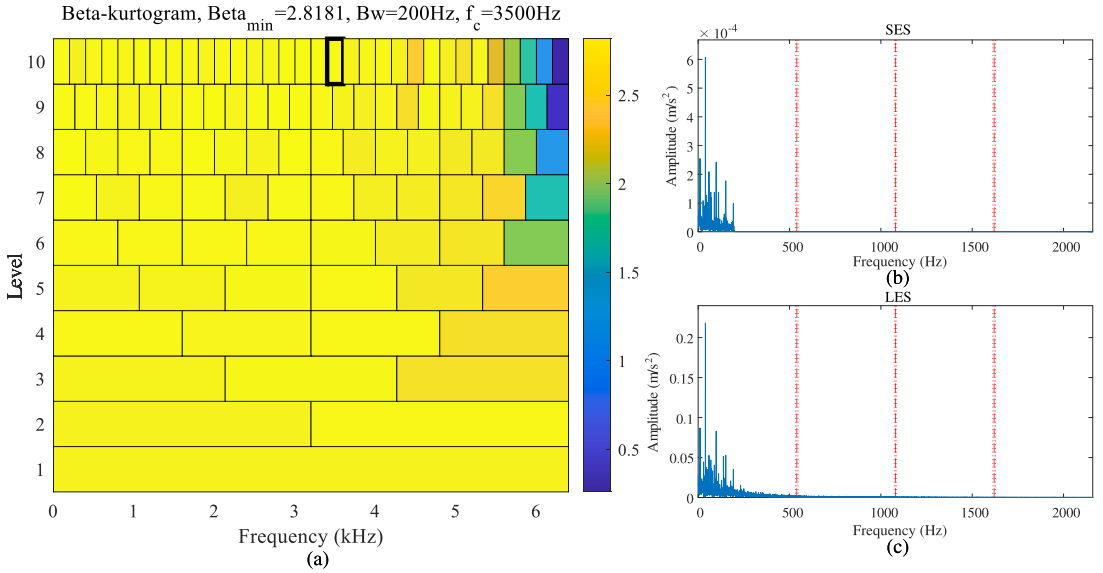

Fig. 33. Raw signal affected by a compound fault of bearings and gears. in Case II: (a) Demodulation band determination via Beta-Kurtogram, (b) Squared envelope spectrum, (c) Logarithmic scale envelope spectral analysis.

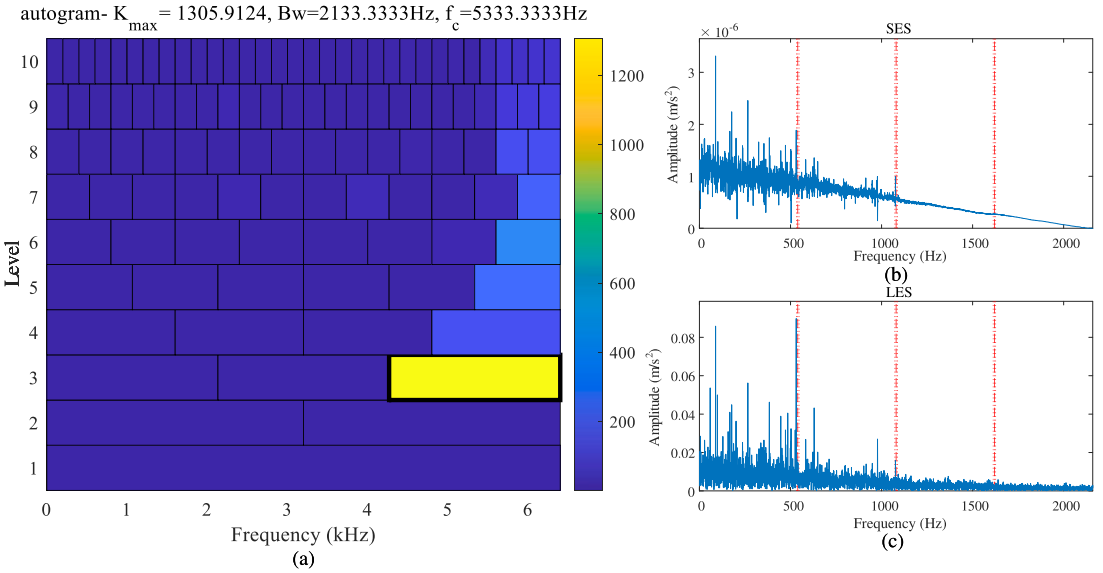

Fig. 34. Raw signal affected by a compound fault of bearings and gears. in Case II: (a) Demodulation band determination via Autogram, (b) Squared envelope spectrum, (c) Logarithmic scale envelope spectral analysis.

selection to separated signals enables a clear delineation of the characteristic frequencies associated with both bearing and gear faults in both spectral representations. Consequently, these findings substantiate the efficacy of the proposed framework, demonstrating its capacity to enhance the performance of demodulation techniques by effectively suppressing cross-fault interference and thereby facilitating more accurate fault identification.

4.3. Case study II

This dataset provides invaluable insights into diverse operational states and fault characteristics, thereby establishing a robust foundation for diagnostic analysis. The experimental apparatus, methodically constructed and precisely configured as illustrated in Fig. 26, integrates multiple critical components into a cohesive testing platform. These essential elements include a high-precision tachometer for accurate speed monitoring, a carefully calibrated drive motor, an advanced torque sensor for load measurement, a sophisticated dual-stage parallel gear assembly, specialized loading gear units, and a precisely controlled load motor.

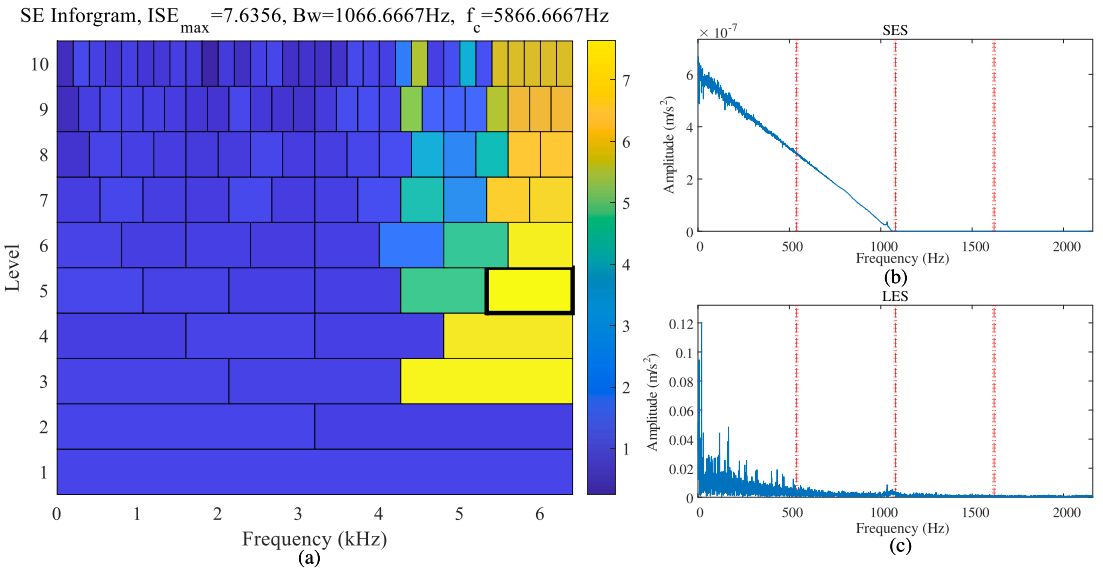

Fig. 35. Raw signal affected by a compound fault of bearings and gears. in Case II: (a) Demodulation band determination via Infogram, (b) Squared envelope spectrum, (c) Logarithmic scale envelope spectral analysis.

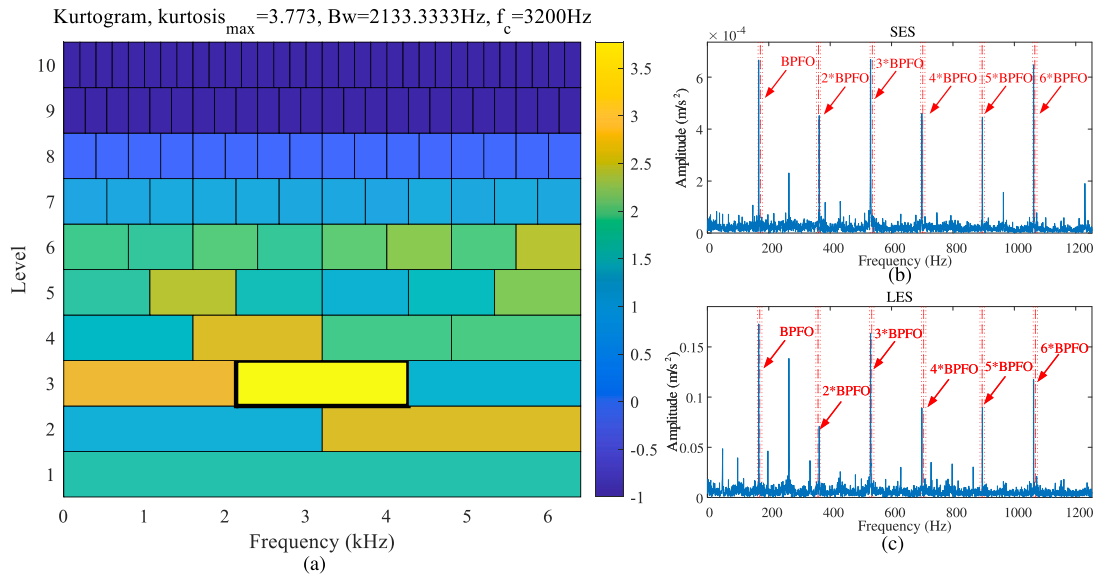

Fig. 36. Case II: (a) Demodulation band determination via Fast-Kurtogram, (b) Squared envelope spectrum, (c) Logarithmic scale envelope spectral analysis.

A distinguishing feature of this experimental configuration lies in the strategic placement of an accelerometer on an isolated disk–an intentional design choice that proves crucial for optimal vibration signal acquisition. The specific mounting configuration of this sensor is comprehensively detailed in the figure's inset, highlighting its significance in the overall experimental framework. To ensure the capture of high-fidelity dynamic behavior and transient phenomena, the system employs an advanced data acquisition protocol operating at 12.8 kHz. This experimental framework systematically encompasses operational speeds ranging from 1000 r/min to 3000 r/min , thereby enabling a thorough investigation across multiple operational regimes. Beyond standard operating conditions, the dataset has been enriched through the deliberate incorporation of sophisticated combined fault scenarios, with particular emphasis on the complex interactions between gear and bearing defects, as comprehensively illustrated in Fig. 27. The internal architecture of the parallel gearbox system, along with its component arrangements, is meticulously illustrated in the same figure. For establishing a statistically robust foundation for fault analysis, vibration measurements of gear tooth breakage and bearing outer race composite faults were recorded along the x-axis of the accelerometer during carefully controlled steady-state operations under a constant rotational speed of 3000 rpm and a constant load of 20 Nm, ensuring the consistency and reliability of the acquired data.

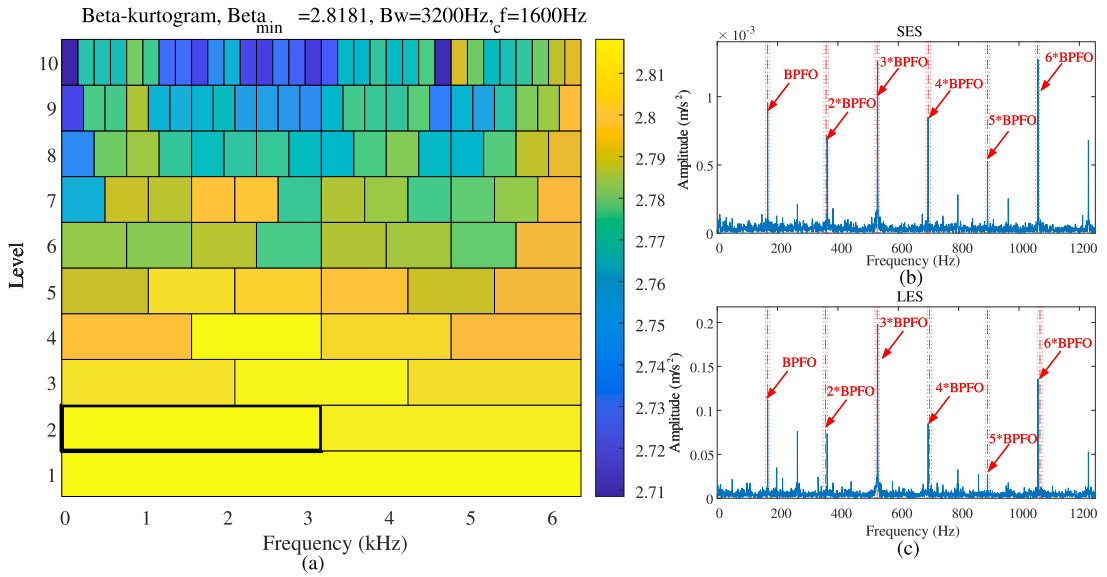

Fig. 37. Case II: (a) Demodulation band determination via Beta-Kurtogram, (b) Squared envelope spectrum, (c) Logarithmic scale envelope spectral analysis.

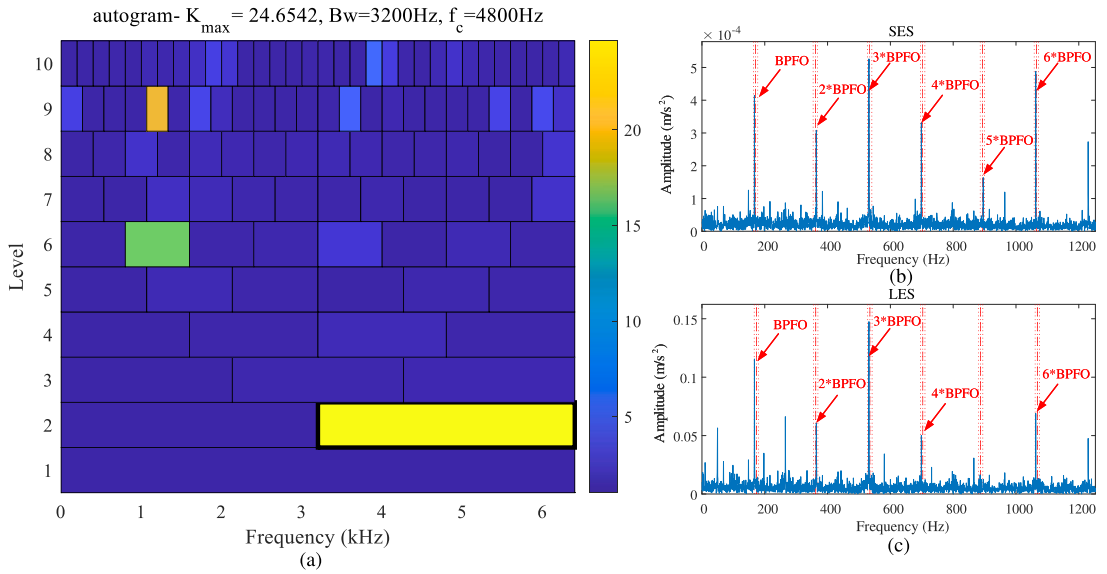

Fig. 38. Case II: (a) Demodulation band determination via Autogram, (b) Squared envelope spectrum, (c) Logarithmic scale envelope spectral analysis.

To validate the efficacy of the proposed methodology, a vibration signal encapsulating compound gear-bearing faults was collected under conditions of steady rotational speed. As represented by the blue waveform in Fig. 28(b), the fault signatures are significantly obscured by a pronounced background of intensified noise, thereby establishing a challenging and robust testing ground for the evaluation of the proposed fault separation framework. This scenario not only underscores the complexity of real-world diagnostic environments but also highlights the critical need for advanced signal processing techniques capable of discerning subtle fault characteristics amidst pervasive interference.

Delving into the specifics of the MED filtering outcomes for the gear fault signal, as illustrated in Fig. 28, the adaptive optimization process, driven by the spectral negentropy criterion (SN-SES), identifies the maximum ΔI_E value at an optimal filter length of $L = 52$, effectively striking a balance between fault feature enhancement and noise suppression in environments dominated by high noise energy. A detailed comparison of time-domain waveforms before and after filtering reveals a marked improvement: the periodic impact features associated with gear faults, initially buried under substantial noise, are brought to the forefront, and although residual noise persists, random signal burrs are considerably diminished, thus enhancing the periodic regularity of fault pulses and affirming the method's precision in isolating gear faults within noisy contexts. Similarly, in the MED filtering analysis of the bearing fault

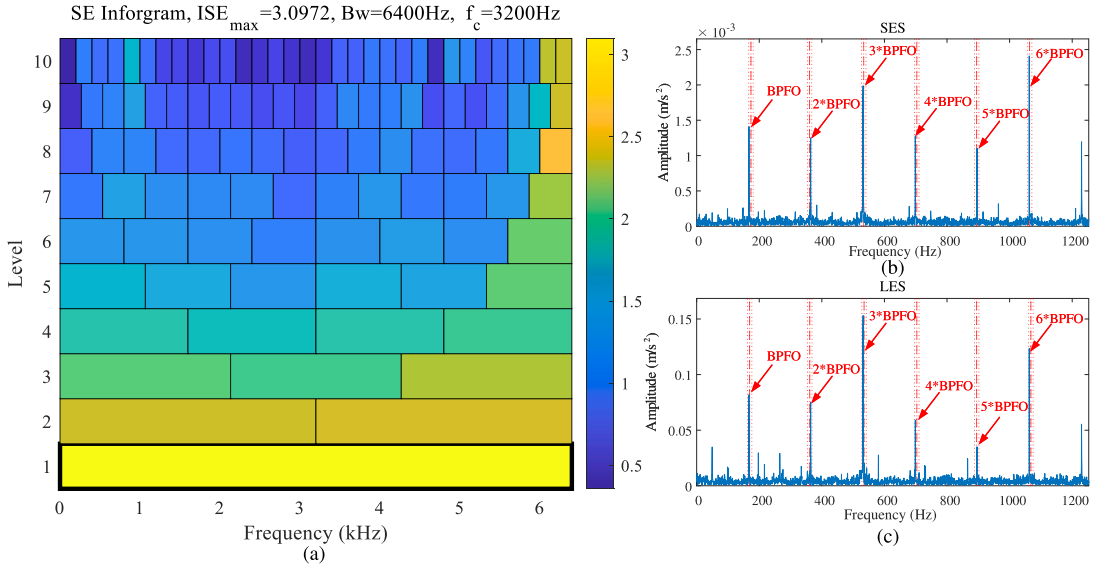

Fig. 39. Case II: (a) Demodulation band determination via Infogram, (b) Squared envelope spectrum, (c) Logarithmic scale envelope spectral analysis.

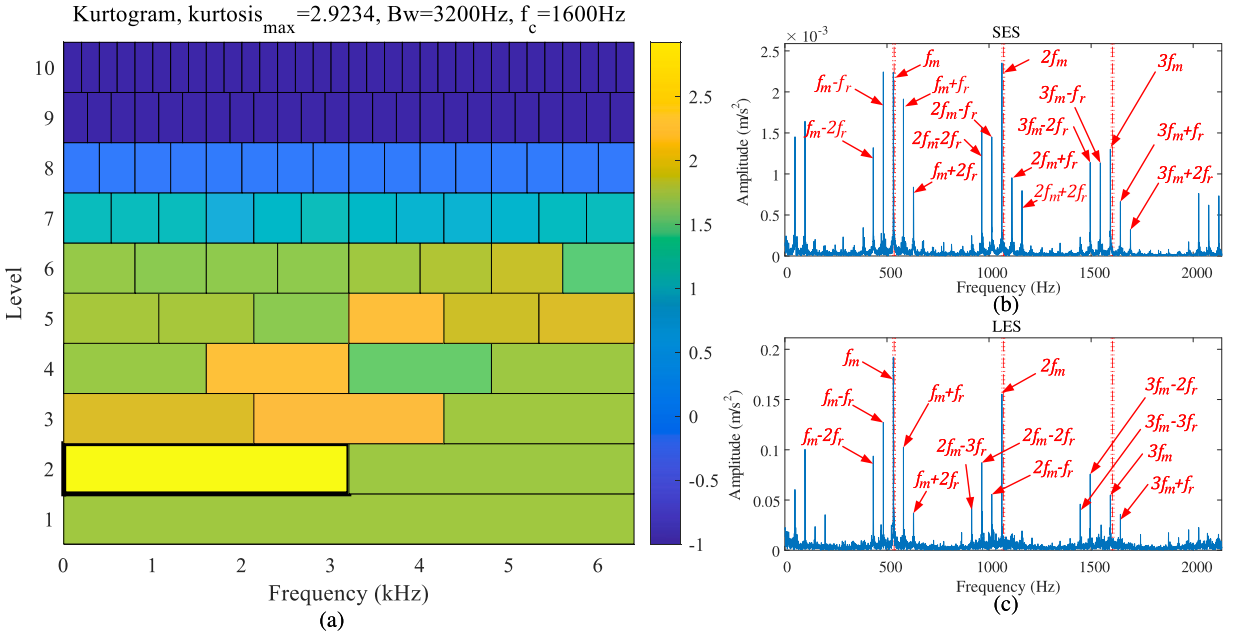

Fig. 40. Case II: (a) Demodulation band determination via Fast-Kurtogram, (b) Squared envelope spectrum, (c) Logarithmic scale envelope spectral analysis.

signal (Fig. 29), a distinct local peak of ΔI_E is observed at an optimal filter length of $L=10$, clearly distinguishable despite the strong noise background. The resulting filtered time-domain waveform demonstrates a significant reduction of high-amplitude gear fault interference to near-noise levels, while successfully extracting the subtle impact features of the bearing inner ring fault from a complex noise floor, thereby evidencing that residual signal analysis is a potent tool for detecting faint fault signatures in high-noise settings.

The enhancement of fault features is achieved through the application of wavelet packet multi-scale optimal correlation kurtosis decomposition and reconstruction, as comprehensively illustrated in Figs. 30 to 31. In the context of gear fault processing (Fig. 30), subbands with high sensitivity, meticulously screened via correlation kurtosis (CK), enable a more precise focus on the periodic meshing impacts characteristic of gear faults. When coupled with Fourier interpolation, the reconstructed signal reveals fault pulses with significantly elevated amplitude levels while compressing noise interference to a minimal threshold. Furthermore, the vibration

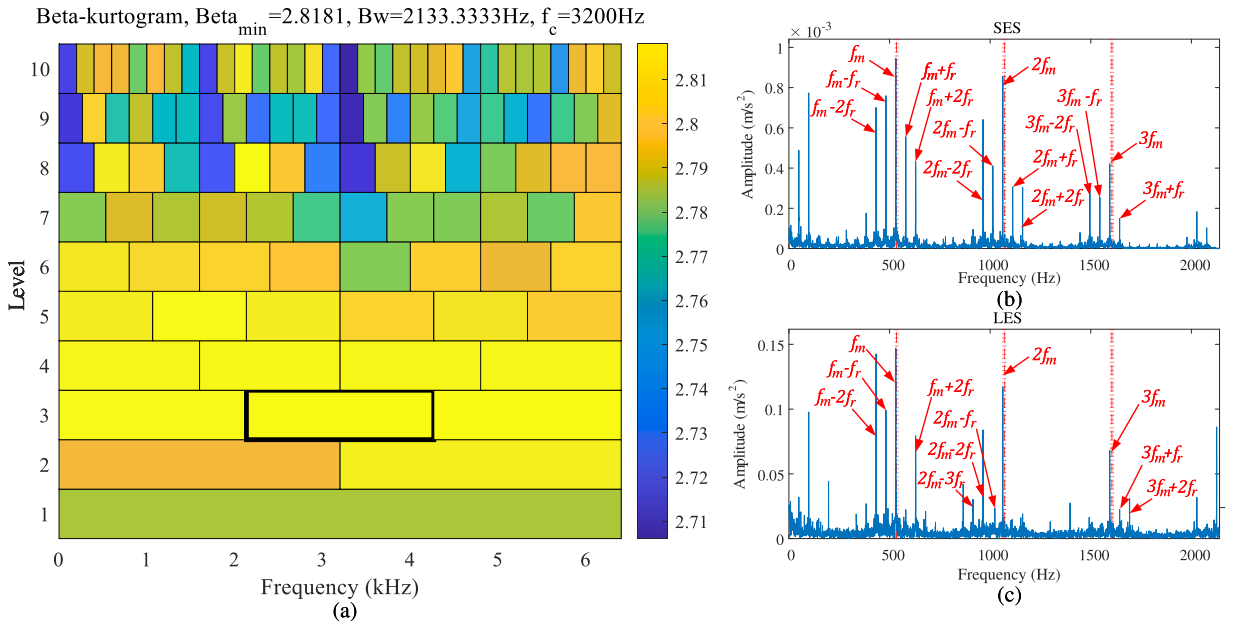

Fig. 41. Case II: (a) Demodulation band determination via Beta-Kurtogram, (b) Squared envelope spectrum, (c) Logarithmic scale envelope spectral analysis.

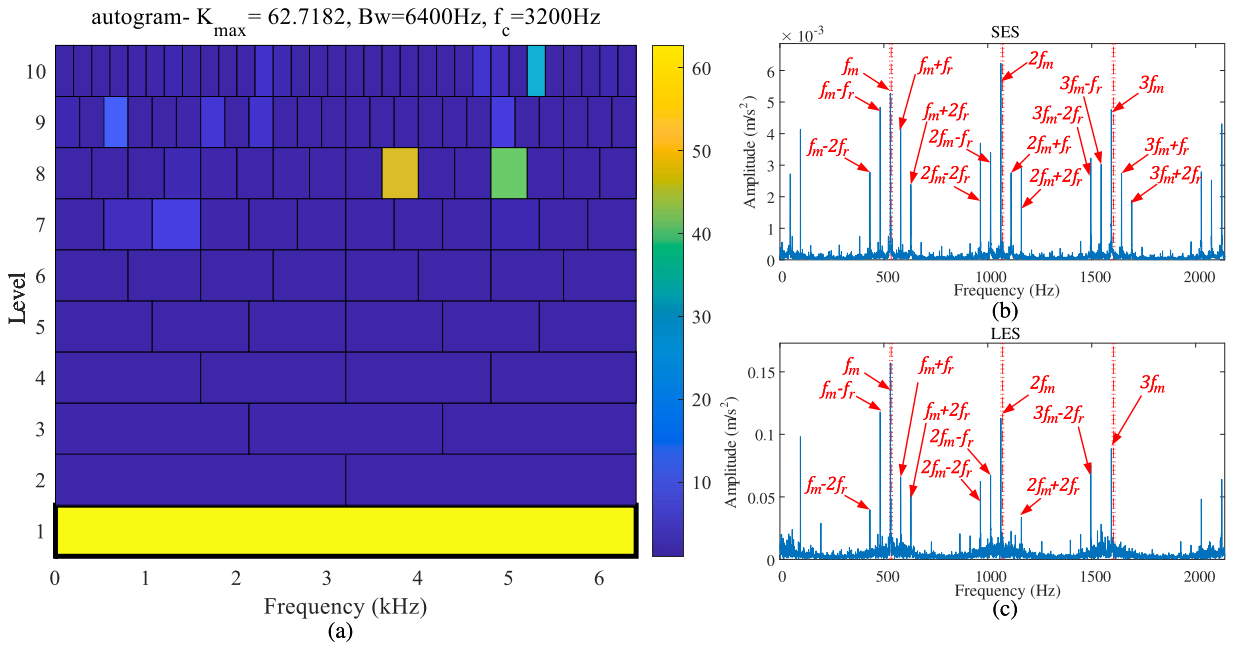

Fig. 42. Case II: (a) Demodulation band determination via Autogram, (b) Squared envelope spectrum, (c) Logarithmic scale envelope spectral analysis.

weight grading adjustment, facilitated by a nonlinear weight function, adeptly isolates noise between fault vibration cycles and amplifies high-level impacts, thereby resulting in gear fault features that manifest as distinct, prominent pulses against a notably clean background, as shown in Fig. 30(b). Similarly, in bearing fault processing (Fig. 31), the integration of wavelet packet decomposition with dynamic window functions ensures accurate locking onto the bearing fault cycle, effectively suppressing gear interference components and preserving the dense impact features of the bearing inner ring fault with remarkable continuity and recognizability, even amidst substantial noise. Collectively, the successful separation of composite fault signals under such challenging conditions robustly substantiates the adaptability and resilience of the proposed framework, affirming its efficacy in extreme noise environments.

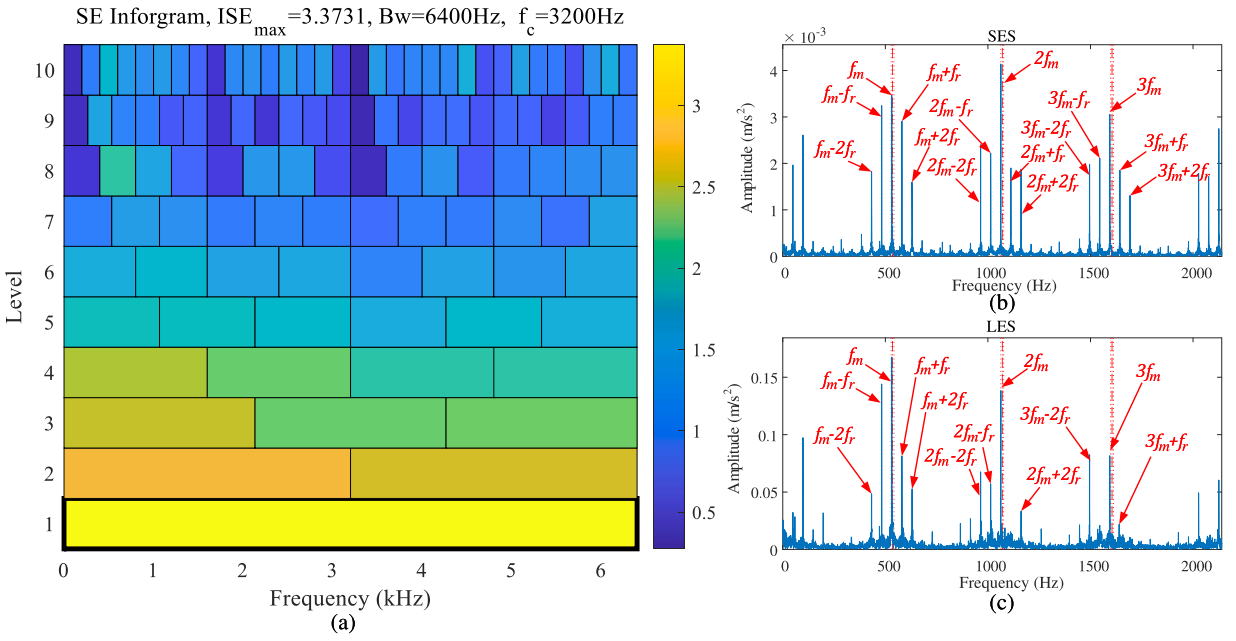

Fig. 43. Case II: (a) Demodulation band determination via Infogram, (b) Squared envelope spectrum, (c) Logarithmic scale envelope spectral analysis.

In a comprehensive experimental analysis focused on gear-bearing compound fault signals amidst significant noise interference, a suite of established signal processing methodologies–namely Fast-Kurtogram, Beta-Kurtogram, Autogram, and Infogram–were rigorously applied across three distinct signal categories: raw composite signals, bearing-separated signals, and gear-separated signals. The findings, meticulously illustrated in Fig. 32 through Fig. 43, emphatically illustrate the pivotal contribution of the proposed noise reduction and signal separation framework. This innovative approach not only mitigates the confounding effects of background noise but also facilitates the precise extraction of fault-specific features, thereby enhancing the diagnostic capability of these techniques in challenging conditions.

The raw composite signals, heavily burdened by elevated noise levels, present formidable obstacles to traditional demodulation strategies, as they struggle to isolate meaningful fault indicators. For instance, Fast-Kurtogram targets a frequency band of [5333.3333Hz, 2133.3333Hz] as shown in Fig. 32(a), whereas Beta-Kurtogram opts for a narrower range of [3500Hz, 200Hz] (Fig. 33(a)). Meanwhile, Autogram aligns with [5333.3333Hz, 2133.3333Hz] (Fig. 34(a)), and Infogram selects [5866.6667Hz, 1066.6667Hz] (Fig. 35(a)). Despite these varied band selections, a critical shortcoming persists across all methods: the Squared Envelope Spectra (SES) in Fig. 32(b), Fig. 33(b), Fig. 34(b) and Fig. 35(b), as well as the Logarithmic Envelope Spectra (LES) in Fig. 32(c), Fig. 33(c), Fig. 34(c) and Fig. 35(c), consistently fail to delineate essential diagnostic markers, such as the bearing outer race fault frequency (BPFO = 179.7Hz), gear meshing frequency (f_m = 540.6Hz) and sideband frequency (f_r = 49.8Hz), all of which remain obscured beneath the dominant noise floor without identifiable peaks or harmonic patterns. This persistent inability to resolve fault signatures starkly highlights the inherent limitations of standalone demodulation techniques when applied to unprocessed signals in high-noise environments, where the confluence of overlapping fault components and pervasive interference effectively conceals critical diagnostic information.

Bearing-separated signals, meticulously preprocessed through the proposed framework, demonstrate exceptional clarity across all four evaluated signal processing techniques, even when employing low-complexity decomposition strategies (ranging from 1 to 3 layers) and relatively broad bandwidths, thus underscoring the robustness of the methodology in challenging diagnostic scenarios. Specifically, Fast-Kurtogram targets a frequency band of [21000Hz, 16000Hz] as depicted in Fig. 36(a), while Beta-Kurtogram refines its selection to a narrower range of [3200Hz, 2133.3333Hz] (Fig. 37(a)), Autogram opts for [26000Hz, 11000Hz] (Fig. 38(a)), and Infogram settles on [24500Hz, 6500Hz] (Fig. 39(a)). The profound effectiveness of this framework becomes strikingly evident in the SES and LES outcomes, as illustrated across multiple figures including Fig. 36(b) and (c), Fig. 37(b) and (c), Fig. 38(b) and (c), as well as Fig. 39(b) and (c), where the bearing outer race fault frequency manifests as a distinct, sharp peak, with harmonics extending beyond the 6th order being clearly discernible. This ability to detect high-order harmonics in noisy environments is a direct result of the framework's superior noise suppression capabilities, which effectively isolate bearing fault components from both gear interference and pervasive background noise. Moreover, despite the use of wideband selections, the pre-separated signals maintain a high degree of purity, facilitating precise demodulation, as each technique's envelope spectra consistently exhibit outstanding signal-to-noise ratios, with 6th-order and higher harmonics retaining diagnostic clarity. Consequently, these results affirm the framework's remarkable capacity to safeguard weak high-order harmonics while simultaneously reducing computational demands through low-level decomposition, thereby accelerating processing times without sacrificing diagnostic accuracy.

The gear-separated signals, when processed through the proposed framework, demonstrate a remarkable consistency in efficacy across all evaluated methodologies, even under conditions of minimal decomposition, thereby highlighting the robustness of the approach. Fast-Kurtogram delineates a frequency band of [1600Hz, 3200Hz] (Fig. 40(a)), while Beta-Kurtogram refines its selection to a narrower range of [3200Hz, 2133.3333Hz] (Fig. 41(a)). In parallel, both Autogram and Infogram converge on a broader band of [3200Hz, 6400Hz] (Figs. 42(a) and 43(a), respectively). Within the corresponding SES and LES spectra, as meticulously presented in Figs. 40(b) and (c), 41(b) and (c), 42(b) and (c), and 43(b) and (c), the gear meshing frequency alongside its higher-order harmonics is sharply resolved, accompanied by a clear depiction of multiple sidebands spaced at the rotational frequency–a phenomenon attributable to gear manufacturing imperfections or load fluctuations. Furthermore, the framework's adaptive separation mechanism proficiently amplifies these subtle modulations while effectively attenuating extraneous noise, thus enabling a precise quantification of fault severity through detailed sideband analysis. Even when employing broad frequency selections, the preprocessed signals preserve ample fault-specific information, facilitating high-fidelity harmonic reconstruction without the burden of computationally intensive deep decomposition. This harmonious balance between bandwidth efficiency and diagnostic precision not only validates the framework's effectiveness but also underscores its scalability and suitability for real-time industrial applications where rapid and accurate fault detection is paramount.

5. Conclusion

In conclusion, the proposed multi-source vibration demodulation framework effectively addresses the longstanding challenges of high-speed rail bogie fault diagnosis, including low signal-to-noise ratio, mode mixing, and the need for laborious hyperparameter tuning. By integrating optimized MCKD with vibration-weighted grading distribution and Latent Cyclic Pattern Discovery, the approach enables adaptive deconvolution, robust weak-impulse extraction, and precise cycle-synchronous feature separation–yielding superior diagnostic accuracy, noise robustness, and computational efficiency compared to conventional MED, MOMEDA, and MCKD techniques. The method's ability to operate without empirical parameter tuning and to recover hidden or time-warped periodicities demonstrates its practical value for real-world bogie monitoring. For future work, several avenues are promising. First, further validation should be conducted across diverse bogie types, operational scenarios, and fault severities to generalize and benchmark performance. Extension of the framework to integrate other sources of sensory data, such as acoustic or thermal signals, could enhance fault discrimination, especially for incipient or compound failure modes. Developing online or edge-optimized implementations would facilitate real-time monitoring in resource-constrained environments. Finally, exploring machine learning-driven adaptivity and transfer learning could further minimize manual configuration while extending applicability to other complex mechanical systems beyond high-speed rail.

CRediT authorship contribution statement

Peng Chen: Writing – review & editing, Writing – original draft, Supervision, Resources, Project administration, Methodology, Investigation, Funding acquisition, Formal analysis, Conceptualization; **Yuhao Wu:** Writing – original draft, Visualization, Validation, Software, Methodology, Investigation, Formal analysis, Data curation; **Junxiao Ma:** Validation, Methodology, Formal analysis, Data curation; **Ruijin Zhang:** Validation, Methodology, Formal analysis, Data curation; **Ge Xin:** Project administration, Methodology, Investigation, Funding acquisition, Conceptualization; **Changbo He:** Supervision, Project administration, Methodology, Investigation, Funding acquisition, Formal analysis.

Data availability

Data will be made available on request.

Declaration of competing interest

The authors declare that they have no known competing financial interests or personal relationships that could have appeared to influence the work reported in this paper.

Acknowledgments

This research was supported by the National Natural Science Foundation of China (Grants 52105111, 52305085, 52375078, and U23B20104), the Guangdong Basic and Applied Basic Research Foundation (Grant 2025A1515012256), the China Postdoctoral Science Foundation (Grant 2023M740021), and the Natural Science Foundation of Anhui Province (Grant 2108085QE229).

References

[1] T. Kim, J. Park, J. Yoo, J.M. Ha, B.D. Youn, Enhancing gearbox fault diagnosis under phase estimation errors: a dynamic time warping and blind deconvolution approach, J. Sound Vib. 598 (2025) 118851.

[2] D. He, J. Wu, Z. Jin, C. Huang, Z. Wei, C. Yi, AGFCN: A bearing fault diagnosis method for high-speed train bogie under complex working conditions, Reliab. Eng. Syst. Saf. 258 (2025) 110907.

[3] S. Li, H. Wang, C. Yan, Y. Hou, L. Wu, A systematic review on diagnosis methods for rolling bearing compound fault: research status, challenges, and future prospects, Meas. Sci. Technol. (2024).
[4] P. Chen, J. Gao, R. Zhang, Y. Jin, R. Yu, C. He, J. Qi, Metric-guided graph contrastive learning: an unsupervised approach for few-shot gearbox fault diagnosis, Meas. Sci. Technol. 36 (7) (2025) 076110.
[5] C. Xu, P. Chen, J. Gao, Y. Jin, M. Rao, Semi-supervised transfer learning preserving spatial homogeneity for gearbox diagnostics in extraneous transient noise, Nondestruct. Test. Eval. (2025) 1–29.
[6] P. Chen, R. Zhang, S. Fan, J. Guo, X. Yang, Step-wise contrastive representation learning for diagnosing unknown defective categories in planetary gearboxes, Knowl. Based Syst. 309 (2024) 112863.
[7] Y. Wang, P. Chen, Q. Wei, J. Qi, C. He, C. Zhou, Multi-channel fusion scale transformed signals with magnetic leakage for damage detection in steel wire ropes, Nondestruct. Test. Eval. (2025) 1–26.
[8] P. Chen, R. Zhang, C. He, Y. Jin, S. Fan, J. Qi, C. Zhou, C. Zhang, Progressive contrastive representation learning for defect diagnosis in aluminum disk substrates with a bio-inspired vision sensor, Expert Syst. Appl. (2025) 128305.
[9] P. Chen, Z. Ma, C. Xu, M. Zhang, H. Li, K. Zheng, Y. Jin, Scale-aware domain adaptation for surface defects detection on machine tool components in contaminant measurements, IEEE Trans. Instrum. Meas. (2025) 1- 9.
[10] D. Peng, X. Zhu, W. Teng, Y. Liu, Use of generalized gaussian cyclostationarity for blind deconvolution and its application to bearing fault diagnosis under non-Gaussian conditions, Mech. Syst. Signal Process. 196 (2023) 110351.
[11] L. Cui, W. Sun, X. Zhao, D. Liu, Adaptive maximum second-order cyclostationarity blind deconvolution based on diagnostic feature spectrum for rolling bearing fault diagnosis, IEEE Trans. Instrum. Meas. (2025).
[12] Y. Cheng, N. Zhou, Z. Wang, B. Chen, W. Zhang, CFFsBd: a candidate fault frequencies-based blind deconvolution for rolling element bearings fault feature enhancement, IEEE Trans. Instrum. Meas. 72 (2023) 1–12.
[13] P. Chen, J. Gao, Y. Jin, C. Zhou, J. Qi, C. He, Physics-Aware digital twin and few-Shot learning for self-Supervised gearbox fault diagnosis, Meas. Sci. Technol. 36 (7) (2025).
[14] P. Chen, Y. Wu, C. Xu, Y. Jin, C. Zhou, Markov modeling of signal condition transitions for bearing diagnostics under external interference conditions, IEEE Trans. Instrum. Meas. 73 (3518308) (2024).
[15] M. Hu, G. Wang, K. Ma, Identification of wind turbine gearbox weak compound fault based on optimal empirical wavelet transform, Meas. Sci. Technol. 34 (4) (2023) 045003.
[16] P. Chen, Y. Wu, C. Xu, C.-G. Huang, M. Zhang, J. Yuan, Interference suppression of non-stationary signals and bearing diagnosis under transient noise environments, IEEE Trans. Reliab. (2024).
[17] Z. Guo, H. Fei, B. Liu, Y. Cao, Sparse representation based on MCKD and periodic dictionary for bearing fault diagnosis, IEEE Trans. Instrum. Meas. 73 (2024) 1–10.
[18] S. Gong, S. Li, M. Xia, Compound fault feature separation with frequency segmentation and improved sparse filtering for rolling bearings, Struct. Health Monitor. (2025) 14759217251320676.
[19] P. Chen, Z. Ma, C. Xu, Y. Jin, C. Zhou, Self-Supervised transfer learning for remote wear evaluation in machine tool elements with imaging transmission attenuation, IEEE Internet Things J. 11 (2024) 23045 - 23054.
[20] P. Chen, Y. Wu, S. Fan, C. He, Y. Jin, J. Qi, C. Zhou, Adaptive signal regime for identifying transient shifts: a novel approach toward fault diagnosis in wind turbine systems, Ocean Eng. 325 (2025) 120798.
[21] R.A. Wiggins, Minimum entropy deconvolution, Geoexploration 16 (1–2) (1978) 21–35.
[22] N. Sawalhi, R.B. Randall, H. Endo, The enhancement of fault detection and diagnosis in rolling element bearings using minimum entropy deconvolution combined with spectral kurtosis, Mech. Syst. Signal Process. 21 (6) (2007) 2616–2633.
[23] G.L. McDonald, Q. Zhao, M.J. Zuo, Maximum correlated kurtosis deconvolution and application on gear tooth chip fault detection, Mech. Syst. Signal Process. 33 (2012) 237–255.
[24] G.L. McDonald, Q. Zhao, Multipoint optimal minimum entropy deconvolution and convolution fix: application to vibration fault detection, Mech. Syst. Signal Process. 82 (2017) 461–477.
[25] M. Buzzoni, J. Antoni, G. d'Elia, Blind deconvolution based on cyclostationarity maximization and its application to fault identification, J. Sound Vib. 432 (2018) 569–601.
[26] N.E. Huang, Z. Shen, S.R. Long, M.C. Wu, H.H. Shih, Q. Zheng, N.-C. Yen, C.C. Tung, H.H. Liu, The empirical mode decomposition and the hilbert spectrum for nonlinear and non-stationary time series analysis, Proceedings of the Royal Society of London. Series A: mathematical, physical and engineering sciences 454 (1971) (1998) 903–995.
[27] N. Rehman, D.P. Mandic, Multivariate empirical mode decomposition, Proceedings of the Royal Society A: Mathematical, Physical and Engineering Sciences 466 (2117) (2010) 1291–1302.
[28] P.C. Chu, C. Fan, N. Huang, Derivative-optimized empirical mode decomposition for the hilbert–Huang transform, J. Comput. Appl. Math. 259 (2014) 57–64.
[29] K. Dragomiretskiy, D. Zosso, Variational mode decomposition, IEEE Trans. Signal Process. 62 (3) (2013) 531–544.
[30] N. Ur Rehman, H. Aftab, Multivariate variational mode decomposition, IEEE Trans. Signal Process. 67 (23) (2019) 6039–6052.
[31] W. Chen, Y. Zhang, A general method for mode decomposition on additive mixture: generalized variational mode decomposition and its sequentialization, Neurocomputing 606 (2024) 128390.
[32] R.R. Coifman, Y. Meyer, S. Quake, M.V. Wickerhauser, Signal processing and compression with wavelet packets, Wavelets Their Appl. (1994) 363–379.
[33] I. Daubechies, The wavelet transform, time-frequency localization and signal analysis, IEEE Trans. Inf. Theory 36 (5) (1990) 961–1005.